Relativistic collapse of Landau levels of Kane fermions in crossed electric and magnetic fields

Sergey S. Krishtopenko[1,*] and Frédéric Teppe[1,2]

[1]*CENTERA Laboratories, Institute of High Pressure Physics, Polish Academy of Sciences, PL-01-142 Warsaw, Poland*

[2]*Laboratoire Charles Coulomb (L2C), UMR 5221 CNRS-Université de Montpellier, F-34095 Montpellier, France*

(Received 10 November 2021; accepted 21 March 2022; published 28 March 2022)

Using an elegant model involving only Γ_{6c} and Γ_{8v} bands, massless Kane fermions were defined as the particles associated with the peculiar band structure of gapless HgCdTe crystals. Although their dispersion relation resembles that of a pseudo-spin-1 Dirac semimetal, these particles were originally considered to be hybrids of pseudospin-1 and -1/2 fermions. Here we unequivocally find that, by considering an additional Γ_{7c} conduction band inherent in HgCdTe crystals, the Kane fermions are ultimately two nested Dirac particles. This observation allows for the direct application of Lorentz transformations to describe the relativistic behavior of these particles in crossed electric and magnetic fields. By studying the relativistic collapse of their Landau levels at different orientations between the crossed fields and the main crystallographic axes, we demonstrate that the Kane fermions strikingly decay into two independent Dirac particles with increase of the electric field. Our results provide insight into semirelativistic effects in narrow-gap semiconductors in crossed electric and magnetic fields.

DOI: 10.1103/PhysRevB.105.125203

I. INTRODUCTION

According to the solutions of the Dirac equation, essential in high energy physics, relativistic particles are classified into Dirac, Majorana, or Weyl fermions. In solids, the interaction of electrons with the periodic potential of the crystal lattice can give rise to dispersion relations at high symmetry points of the Brillouin zone, which mimic the relativistic particles.

This relativistic analogy is usually used for materials, in which conduction and valence bands are well separated from the other bands, considered as the remote bands. In the early 1960s, Keldysh [1] and Wolff [2] independently discovered that the two-band description of the bismuth-, PbTe-, PbSe-, and PbS-type semiconductors was equivalent to the Dirac equation for free particles. If the band gap vanishes, the band structure mimics either by massless Dirac fermions or Weyl fermions. Solid state analogs of massless relativistic particles were demonstrated in graphene [3], semiconductor quantum wells [4–8], topological insulators [9–11], Dirac [12–15], and Weyl [16–18] semimetals.

One of the relativistic properties of spin-1/2 fermions, which can also be probed in "nonrelativistic" solids, arises in the presence of perpendicular electric and magnetic fields. Aronov and Pikus [19,20] on the one hand and Zawadzki and Lax [21,22] on the other hand utilized this relativistic analogy to describe the inter-Landau level transitions within a two-band approximation in crossed electric $\mathcal{E}$ and magnetic $\mathcal{B}$ fields. Particularly, Aronov and Pikus [19,20] were the first who proposed to apply the Lorentz transformation with "an effective speed of the light" to eliminate the magnetic field when $\mathcal{E} > \mathcal{B}$ in the moving coordinate system and the electric field when $\mathcal{E} < \mathcal{B}$. In the former case, the particle motion is infinite and no quantization takes place, while in the latter case the Landau quantization remains until its collapse when the drift velocity $V_d = c\mathcal{E}/\mathcal{B}$ (where c is the speed of light in vacuum) reaches the effective speed of the light $\tilde{c}$ in the system. Forty years later, similar results were obtained for graphene [23]. Note that the effective speed of the light in solids represents the maximum particle velocity in the system—for instance, the Fermi velocity in graphene [3].

A fundamental difference between electrons in solids and those at high energy is that Lorentz invariance is not always preserved in condensed matter physics. By generalizing the Dirac equation, one can find many other free fermionic excitations that have no high-energy analogs [24–27]. Massless "pseudo-spin-1 and -3/2" Dirac and Weyl fermions are a remarkable example of such particles, whose low-energy Hamiltonian has the form of $\mathbf{k} \cdot \mathbf{S}$, where $\mathbf{S}$ is the vector of spin-1 or -3/2 matrices.

Massless Kane fermions, observed in gapless HgCdTe crystals [28,29], represent another type of fermionic excitations formed by the crossing of three bands. Its unique band structure is characterized by doubly degenerate conical bands intersected at the vertex by an additional flat band, closely resembling a pseudo-spin-1 Dirac semimetal [27]. However, unlike the pseudo-spin-1 Dirac fermions, Kane fermions are not protected by symmetry or topology, and their band structure can be set at will [29]. The discussion of the nature of Kane fermions has become more confusing after Malcolm and Nicol [30], who noted that the three-band Kane Hamiltonian involving the Γ_{8v} and Γ_{6c} bands maps onto an intermediate value ($\alpha = 1/\sqrt{3}$) of the α-$\mathcal{T}_3$ model [31]. Since the α-$\mathcal{T}_3$ model interpolates between the spin-1/2 (graphene, $\alpha = 0$) and pseudo-spin-1 (dice or $\mathcal{T}_3$ lattice, $\alpha = 1$) Dirac-Weyl systems, it was concluded that the

*sergey.krishtopenko@gmail.com

Kane fermions are hybrids of pseudo-spin-1 and -1/2 Dirac fermions.

In this work, by taking into account an additional conduction Γ_{7c} band resulting in a finite curvature of the heavy-hole band in HgCdTe crystals, we unequivocally identify the Kane fermions as spin-1/2 particles. Furthermore, using this extended (3+1)-band model, we show that the Kane fermion is composed of two *mutually hybridized* Dirac particles. This representation makes it possible to directly apply the Lorentz transformation for the calculation of the Landau levels in crossed electric and magnetic fields. We have found that increasing the electric field first leads to the decay of the Kane fermion into two independent Dirac particles. Then, the Landau levels of the Dirac particles collapse when their drift velocities V_d reach the value V_d^* lying between *half* and *full* value of the effective speed of the light. This is a distinctive feature of Kane fermions, since the Landau levels of conventional Dirac fermions normally collapse as V_d approaches the effective speed of light [19–23]. In addition, this limiting speed depends on the orientation of the electric and magnetic fields with respect to the main crystallographic axes of the zinc-blende crystals.

The paper is organized as follows. In Sec. II, we briefly review the existing three-band description of Kane fermions in crossed electric and magnetic fields. In Sec. III, we describe the main consequences of taking into account the additional $|\Gamma_{7c}, \pm 1/2\rangle$ band. Subsequently, we consider in detail the application of the Lorentz transformation allowing us to eliminate the electric field in the moving reference frame for two orientations of the magnetic field ($\mathcal{B} \parallel [001]$ and $\mathcal{B} \parallel [010]$) resulting in various conditions of Landau level collapse. Section IV provides the comparison between Dirac and Kane fermions in crossed electric and magnetic fields and a discussion on the Landau level collapse in HgCdTe bulk crystals with inverted and noninverted band structure. Finally, the main results are summarized in Sec. V.

II. BRIEF OVERVIEW OF THE PROBLEM

Let us first briefly overview the three-band description of Kane fermions [28,29], which until now has allowed them to be considered as hybrids of pseudospin-1 and -1/2 fermions. Up to first order in $\mathbf{k}\cdot\mathbf{p}$ theory, the three-band Hamiltonian involving the Γ_{6c} and Γ_{8v} bands can be presented in the form [32]

$$\hat{\mathcal{H}}_{6\times6}(\mathbf{k},\theta) = \begin{pmatrix} \hat{\mathcal{H}}_0(k_x,k_y,\theta) & \hat{\mathcal{H}}_z(k_z) \\ \hat{\mathcal{H}}_z(k_z)^\dagger & \hat{\mathcal{H}}_0^*(-k_x,-k_y,\theta) \end{pmatrix}, \quad (1)$$

where the asterisk stands for complex conjugation and "†" corresponds to Hermitian conjugation. The 3×3 blocks $\hat{H}_0(k_x,k_y,k_z)$ and $\hat{H}_z(k_z)$ in Eq. (1) are written as

$$\hat{H}_0 = \begin{pmatrix} C_0+M_0 & Vk_+\sin\theta & Vk_-\cos\theta \\ Vk_-\sin\theta & C_0-M_0 & 0 \\ Vk_+\cos\theta & 0 & C_0-M_0 \end{pmatrix} \quad (2)$$

and

$$\hat{H}_z = \begin{pmatrix} 0 & 0 & Vk_z \\ 0 & 0 & 0 \\ Vk_z & 0 & 0 \end{pmatrix}, \quad (3)$$

where $k_\pm = k_x \pm ik_y$ with k_x, k_y, k_z being momentum operators, C_0 is an energy reference, $V/\hbar$ is the effective speed of the light $\tilde{c}$ related with the momentum matrix element P between the Γ_{6c} and Γ_{8v} bands [28], and M_0 is the mass parameter describing the ordering of Γ_{6c} and Γ_{8v} bands [29]. In Eq. (2), we have additionally introduced a "hybridization angle" θ describing the mixing between light and heavy holes at finite quasimomentum [32]. For the Kane fermions, $\theta = \pi/3$. Since $\hat{\mathcal{H}}_{6\times6}(\mathbf{k},\theta)$, $\hat{\mathcal{H}}_{6\times6}(\mathbf{k},-\theta)$, and $\hat{\mathcal{H}}_{6\times6}(\mathbf{k},\pi/2\pm\theta)$ in the absence of magnetic field are all related by unitary transformation, one can only consider the θ values within the range $[0,\pi/2)$.

As first noted by Malcolm and Nicol [30], the Hamiltonian in Eq. (1) at $k_z = 0$ and $M_0 = 0$ is nothing but two copies of the α-$\mathcal{T}_3$ model [31] interpolating between the spin-1/2 and pseudo-spin-1 Dirac-Weyl systems. In our notation, $\hat{\mathcal{H}}_{6\times6}(\mathbf{k},\theta)$ describes the physics of graphene (dice lattice) at $\theta = 0$ ($\theta = \pi/4$), where two diagonal blocks pertain to the distinct chiral centers K and K', respectively [31]. In the 3D case, nonzero k_z takes the role of connecting two otherwise independent chiral blocks.

An inherent feature of $\hat{\mathcal{H}}_{6\times6}(\mathbf{k},\theta)$ is the independence of its eigenvalues from θ, that makes the Kane fermion energy dispersion ($\theta = \pi/3$) the same as the one of the Dirac fermion ($\theta = 0$) with independent flat band:

$$E_\pm(\mathbf{k}) = C_0 \pm \sqrt{M_0^2 + V^2k^2}, \quad E_0 = C_0 - M_0, \quad (4)$$

where $k^2 = k_x^2 + k_y^2 + k_z^2$. However, the difference between Kane and Dirac fermions arises in the presence of a magnetic field. Assuming the orientation of magnetic field $\mathcal{B}$ in the z direction, the Landau level energies are written in the form

$$E_\pm^{(\sigma)} = C_0 \pm \sqrt{M_0^2 + V^2k_z^2 + \frac{2V^2}{a_B^2}(n+1+\sigma\ \sin^2\theta)},$$
$$E_0 = C_0 - M_0, \quad (5)$$

where $n \geqslant -1$ is the Landau level index, $\sigma = -1$ for $n \geqslant 0$, while $\sigma = +1$ for $n \geqslant -1$, and a_B is the magnetic length ($a_B^2 = c\hbar/e\mathcal{B}$, where c is the speed of light in vacuum). As seen from Eq. (5), Landau levels of the Dirac fermion are doubly degenerate at $n \geqslant 0$, while the degeneracy is lifted for the Kane fermion case.

The first attempt to solve the problem of particle motion in crossed fields within the three-band approximation was made by Zawadzki *et al.* [33,34] in the context of InSb semiconductor ($M_0 > 0$). In their work, *neglecting* the electric-field-induced interband terms arising for the squared Hamiltonian $\hat{\mathcal{H}}_{6\times6}(\mathbf{k},\theta)$, the Landau level energies for the Γ_6 band were written as

$$E_{\Gamma_6} = C_0 + \hbar V_d k_y + \sqrt{1-\delta^2}\Bigg[M_0^2 + V^2k_z^2 + \sqrt{1-\delta^2}\frac{2V^2}{a_B^2}\left(n' + \frac{1}{2} + \frac{\sigma'}{4}\right)\Bigg]^{1/2}, \quad (6)$$

where V_d is a drift velocity ($V_d = c\mathcal{E}/\mathcal{B}$), $n' \geqslant 0$ is the Landau level index, and $\sigma' = \pm1$ for all values of n'. In order to obtain this expression in our notations from those of Ref. [33], one has to use the following expressions for the band gap ϵ_g, the

effective mass m_0^*, and the spin-splitting factor g_0^* at the band edge [34]:

$$\epsilon_g = 2M_0, \quad m_0^* = \frac{\hbar^2 M_0}{V^2}, \quad g_0^* = -\frac{m_0}{m_0^*}, \tag{7}$$

where m_0 is the free-electron mass.

The most important quantity in Eq. (6) is δ defined as $\delta = \hbar V_d/V = (c\hbar\mathcal{E})/(V\mathcal{B})$. In deriving Eq. (6), it was assumed that the electric field $\mathcal{E}$ is oriented along the x axis. As seen, the results of Zawadzki *et al.* [33,34] are very similar to the case of Dirac fermions [19–23]—the Landau levels collapse when V_d approaches the effective speed of the light, $\tilde{c} = V/\hbar$. By redefining n' and σ', E_{Γ_6} in Eq. (6) in the absence of electric field is reduced to $E_+^{(\sigma)}$ in Eq. (5) at $\theta = \pi/3$.

Let us now show that the assumptions made by Zawadzki *et al.* in the derivation of Eq. (6) are equivalent to the semiclassical quantization rule for $E_\pm(\mathbf{k})$ in Eq. (4). According to the generalization of the Lifshitz-Onzager quantization rule made by Lifshitz and Kaganov [35], semiclassical Landau levels in crossed electric and magnetic fields can be found from the relation

$$\mathcal{S}(\varepsilon^*, k_z) = \frac{2\pi}{a_B^2}(n+\gamma), \tag{8}$$

where γ is constant and $\mathcal{S}(\varepsilon^*, k_z)$ is the cross section of the surface $E(\mathbf{k}) - \hbar V_d k_y = \varepsilon^*$ in the momentum space. This generalization is due to the fact that in the crossed fields, instead of the energy, the quantity $E(\mathbf{k}) - \hbar V_d k_y =$ is conserved. The latter is nothing but an ellipse in the momentum space

$$V^2 k_x^2 + \left(V^2 - \hbar^2 V_d^2\right)\left[k_y - \frac{\hbar V_d}{V^2 - \hbar^2 V_d^2}(\varepsilon^* - C_0)\right]^2 = \frac{V^2}{V^2 - \hbar^2 V_d^2}(\varepsilon^* - C_0)^2 - M^2 - V^2 k_z^2. \tag{9}$$

By calculation of the ellipse cross section, the energies of the semiclassical Landau levels are written as

$$E_\pm = C_0 + \hbar V_d k_y \pm \sqrt{1-\delta^2}\left[M_0^2 + V^2 k_z^2 + \sqrt{1-\delta^2}\frac{2V^2}{a_B^2}(n+\gamma)\right]^{1/2}, \tag{10}$$

where γ can be defined from the comparison of Eq. (10) at $\delta = 0$ with Eq. (5). The latter makes E_+ equivalent to E_{Γ_6} in Eq. (6).

The main problem of the three-band approximation in crossed electric and magnetic fields manifests itself when one cannot neglect the interband coupling. For the Γ_{6c} band, this arises when M_0^2 becomes comparable with $\beta\hbar^2 V^2 \cos\theta/a_B^2$ and $\beta\hbar^2 V^2 \sin\theta/a_B^2$, which represent the coupling strength with the light- and heavy-hole bands, respectively. On the contrary, for the Γ_{8v} band, the interband coupling is always relevant due to the proximity of the light- and heavy-hole bands. Thus the impossibility of neglecting the interband coupling in materials such as HgCdTe makes it impossible to clearly understand the behavior of Landau levels at relatively high electric fields. The problem is however less challenging beyond the three-band approximation, in which the heavy hole band is flat.

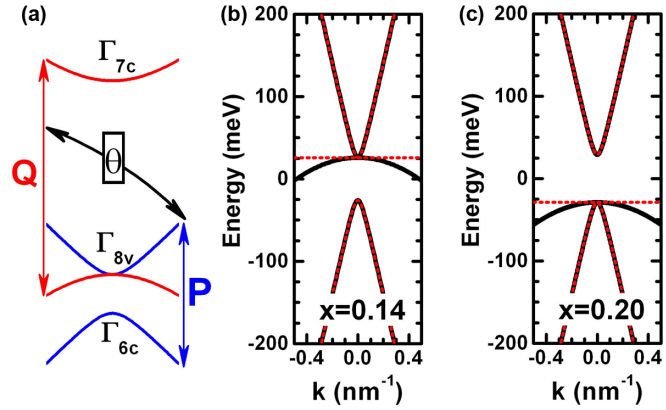

FIG. 1. (a) Schematic representation of the (3+1)-band model as two coupled Dirac systems described by "hybridization angle" θ [32] (for zinc-blende crystal, $\theta = \pi/3$). The "effective speed of light" in each system is determined by the corresponding momentum matrix element P or Q. As shown in Appendix A, for narrow-gap HgCdTe crystals, one can assume $V = \sqrt{2/3}P = \sqrt{2/3}Q$. (b),(c) Band dispersion of $Hg_{1-x}Cd_xTe$ bulk crystals in the three-band (in dotted red) and (3+1)-band (in solid black) models. For the latter case, the second conduction Γ_{7c} band is high in energy lying beyond the figures' scale and $\mathbf{k}$ is oriented along the [100] crystallographic direction.

III. LORENTZ BOOST IN (3+1)-BAND MODEL

To overcome the problems resulting from the three-band approximation, we propose to consider an additional conduction band, whose $\mathbf{k}\cdot\mathbf{p}$ interaction induces the nonzero curvature of the heavy hole band. For the zinc-blende materials, this is the second conduction $|\Gamma_{7c}, \pm 1/2\rangle$ band [36–38]. Further, we briefly outline the main consequences of taking into account the $|\Gamma_{7c}, \pm 1/2\rangle$ band, while a more rigorous derivation of their proper (3+1)-band Hamiltonian from the 14×14 $\mathbf{k}\cdot\mathbf{p}$ model [36–38] of cubic semiconductors can be found in Appendix A.

The first point is that the $|\Gamma_{6c}, \pm 1/2\rangle$–$|\Gamma_{8v}, \pm 1/2\rangle$ and $|\Gamma_{7c}, \pm 1/2\rangle$–$|\Gamma_{8v}, \pm 3/2\rangle$ band pairs represent two Dirac subsystems (see Fig. 1), each described by the *anisotropic* relativistic 3D Dirac Hamiltonian:

$$\hat{\mathcal{H}}_D^{(1,2)}(\mathbf{k}) = C_{1,2}\mathcal{I}_4 + M_{1,2}\alpha_0 + V\cos\theta(k_x\alpha_x + k_y\alpha_y) + Vk_z\alpha_z, \tag{11}$$

where θ is the hybridization angle origin from the mixing between light and heavy holes at nonzero quasimomentum [32], $\mathcal{I}_4$ is a 4×4 identity matrix, and the α matrices are related to the Pauli matrices as

$$\alpha_0 = \begin{pmatrix} \sigma_0 & 0 \\ 0 & -\sigma_0 \end{pmatrix}, \quad \alpha_{x,y,z} = \begin{pmatrix} 0 & \sigma_{x,y,z} \\ \sigma_{x,y,z} & 0 \end{pmatrix}. \tag{12}$$

Here, the forth Pauli matrix σ_0 is defined as a 2×2 identity matrix. In Eq. (11), the constants $C_{1,2}$ and mass parameters $M_{1,2}$ are defined by the energies of $|\Gamma_{6c}, \pm 1/2\rangle$, $|\Gamma_{8v}, \pm 1/2\rangle$, $|\Gamma_{7c}, \pm 1/2\rangle$, and $|\Gamma_{8v}, \pm 3/2\rangle$ bands:

$$C_1 + M_1 = E_{6c}, \quad C_1 - M_1 = E_{8v}, \quad C_2 + M_2 = E_{7c}, \quad C_2 - M_2 = E_{8v}. \tag{13}$$

The last expression determines the position of the heavy-hole band at $\mathbf{k} = 0$. For the case of uniaxially strained HgCdTe or Cd_3As_2, $C_2 - M_2 = E_{8v} + \delta_\epsilon$, where δ_ϵ represents the gap between the light- and heavy-hole subbands [39].

The second point is that the two Dirac subsystems are coupled because of the inevitable hybridization between $|\Gamma_{8v}, \pm 1/2\rangle$ and $|\Gamma_{8v}, \pm 3/2\rangle$ bands in cubic semiconductors. By introducing the hybridization angle θ (see also Sec. II), the generalized (3+1)-band Hamiltonian is written as

$$\hat{\mathcal{H}}_{8\times8}^{(3+1)}(\mathbf{k}) = \begin{pmatrix} \hat{\mathcal{H}}_D^{(1)}(\mathbf{k}) & V\ \sin\theta(k_x\beta_y - k_y\beta_x) \\ V\ \sin\theta(k_y\beta_x - k_x\beta_y) & \hat{\mathcal{H}}_D^{(2)}(\mathbf{k}) \end{pmatrix}, \tag{14}$$

where we have introduced the β matrices as

$$\beta_0^{(z)} = \begin{pmatrix} i\sigma_z & 0 \\ 0 & -i\sigma_z \end{pmatrix}, \quad \beta_{x,y} = \begin{pmatrix} 0 & \sigma_{y,x} \\ -\sigma_{y,x} & 0 \end{pmatrix}. \tag{15}$$

Note the indices order in the definition of β_x and β_y.

The (3+1)-band Hamiltonian in Eq. (14) shows that Kane fermions in HgCdTe can be indeed treated as a combination of two mutually hybridized Dirac particles, which is a direct proof of their pseudorelativistic origin as spin-1/2 particles. This consideration is lacking in the treatment of Kane fermions with the three-band Hamiltonian $\hat{\mathcal{H}}_{6\times6}(\mathbf{k}, \theta)$ in Eq. (1). In its turn, $\hat{\mathcal{H}}_{6\times6}(\mathbf{k}, \theta)$ can be directly obtained from Eq. (14) by projecting $\hat{\mathcal{H}}_{8\times8}^{(3+1)}(\mathbf{k})$ on the $\Gamma_{6c} + \Gamma_{8v}$ subspace in the limit of $E_{7c} - E_{8v} \to \infty$. Comparison of the energy dispersion for $Hg_{0.14}Cd_{0.86}Te$ and $Hg_{0.20}Cd_{0.90}Te$ bulk crystals ($C_1 = 0$, $\theta = \pi/3$) calculated within $\hat{\mathcal{H}}_{6\times6}(\mathbf{k}, \theta)$ and $\hat{\mathcal{H}}_{8\times8}^{(3+1)}(\mathbf{k})$ is provided in Fig. 1. The band parameters for this case can be obtained on the basis of Appendix A and Ref. [39]. Note that, in contrast to $\hat{\mathcal{H}}_{6\times6}(\mathbf{k}, \theta)$, for which $\hat{\mathcal{H}}_{6\times6}(\mathbf{k}, \pm\theta)$ and $\hat{\mathcal{H}}_{6\times6}(\mathbf{k}, \pi/2 \mp \theta)$ in the absence of magnetic field are related by unitary transformation, the extended (3+1)-band Hamiltonian $\hat{\mathcal{H}}_{8\times8}^{(3+1)}(\mathbf{k})$ does not hold this property.

Let us now dwell on several questions related to the (3+1)-band Hamiltonian. First, Eq. (14) corresponds to the Cartesian axes x, y, z oriented along [100], [010], and [001], respectively. For other orientations of the Cartesian axes, the form of $\hat{\mathcal{H}}_{8\times8}^{(3+1)}(\mathbf{k})$ differs from Eq. (14) (see Appendix B). Secondly, one can see that $\hat{\mathcal{H}}_{8\times8}^{(3+1)}(\mathbf{k})$ does not hold the spherical rotational symmetry. This means that Landau levels of the system depend on the orientation of electric and magnetic fields with respect to the main crystallographic orientations. Further, we consider two different cases, in which Landau levels collapse under different conditions.

A. $\mathcal{B} \parallel$ [001]

Let us now consider the behavior of the Kane fermion in constant crossed electric and magnetic fields, when the magnetic field is oriented along [001] direction chosen as the z axis, while the x and y axes are tilted at an angle ϕ from the [100] and [010] directions. In the Cartesian coordinate system, $\hat{\mathcal{H}}_{8\times8}^{(3+1)}(\mathbf{k})$ is written as (see Appendix B)

$$\hat{\mathcal{H}}_{8\times8}^{(3+1)}(\mathbf{k}) = \begin{pmatrix} \hat{\mathcal{H}}_D^{(1)}(\mathbf{k}) & V\ \sin\theta\hat{\mathcal{K}}(\mathbf{k}) \\ -V\ \sin\theta\hat{\mathcal{K}}(\mathbf{k}) & \hat{\mathcal{H}}_D^{(2)}(\mathbf{k}) \end{pmatrix}, \tag{16}$$

where $\hat{\mathcal{H}}_D^{(1,2)}(\mathbf{k})$ takes the form of Eq. (11), while $\hat{\mathcal{K}}(\mathbf{k})$ is written as

$$\hat{\mathcal{K}}(\mathbf{k}) = (k_x\beta_y - k_y\beta_x)\cos2\phi - (k_x\beta_x + k_y\beta_y)\sin2\phi. \tag{17}$$

Assuming the orientation of electric field $\mathcal{E}$ in the x direction and magnetic field $\mathcal{B}$ in the z direction, one has to add the diagonal term $e\mathcal{E}x\mathcal{I}_8$ ($\mathcal{I}_8$ is a 8×8 identity matrix) to $\hat{\mathcal{H}}_{8\times8}^{(3+1)}(\mathbf{k})$ and simultaneously make the Peierls substitution:

$$k_x \to \hat{k}_x = -i\frac{\partial}{\partial x}, \quad k_y \to k_y + \frac{x}{a_B^2}, \tag{18}$$

where a_B is the magnetic length ($a_B^2 = c\hbar/e\mathcal{B}$, where c is the speed of light in vacuum). Then, introducing the "time-momentum" operator as $k_t = -i\hbar\partial/\partial(V_F t)$, the Schrödinger equation for the Kane fermion in crossed fields is written as

$$\left[\hat{\mathcal{H}}_{8\times8}^{(3+1)}(\hat{k}_x, k_y, k_z) + (V_F k_t + e\mathcal{E}x)\mathcal{I}_8\right]|\Psi_{8\times8}\rangle = 0, \tag{19}$$

where, for the sake of brevity, we have introduced $V_F = V\ \cos\theta$.

In order to find the energies E and the wave function $|\Psi_{8\times8}\rangle$ of the Kane fermion, it is convenient to boost to a frame of reference moving with a velocity perpendicular to $\mathcal{E}$ and $\mathcal{B}$. This is performed by means of a Lorentz boost in the y direction on the space-time coordinate system

$$\begin{pmatrix} k_t' \\ k_y' \end{pmatrix} = \begin{pmatrix} \cosh\alpha & \sinh\alpha \\ \sinh\alpha & \cosh\alpha \end{pmatrix}\begin{pmatrix} k_t \\ k_y \end{pmatrix}. \tag{20}$$

Under the Lorentz boost, the wave function transforms, $|\Psi_{8\times8}'\rangle = \mathcal{N}\cdot L_{8\times8}^{(y)}(\alpha)|\Psi_{8\times8}\rangle$, where $L_{8\times8}^{(y)}(\alpha) = \sigma_0 \otimes \exp(\alpha_y \cdot \alpha/2)$, and $\mathcal{N}$ is a normalization constant required since $L_{8\times8}^{(y)}(\alpha)$ does not preserve the norm of the wave function.

Applying the above transformations and choosing

$$\tanh\alpha = -\beta = -\frac{c\hbar}{V}\frac{\mathcal{E}}{\mathcal{B}\cos\theta}, \quad \cosh\alpha = \gamma = \frac{1}{\sqrt{1-\beta^2}}, \tag{21}$$

the Schrödinger equation in Eq. (19) can be rewritten as

$$\left[\begin{pmatrix} \hat{\mathcal{H}}_1' & V_F\tan\theta\hat{\mathcal{K}}' \\ -V_F\tan\theta\hat{\mathcal{K}}' & \hat{\mathcal{H}}_2' \end{pmatrix} + V_F k_t'\begin{pmatrix} \mathcal{I}_4 & -\beta\gamma\ \tan\theta\hat{\mathcal{K}}_t' \\ \beta\gamma\ \tan\theta\hat{\mathcal{K}}_t' & \mathcal{I}_4 \end{pmatrix}\right]|\Psi_{8\times8}'\rangle = 0, \tag{22}$$

where $\hat{\mathcal{H}}_{1,2}'$ are the "boosted" Dirac Hamiltonians:

$$\hat{\mathcal{H}}_{1,2}' = \gamma C_{1,2}(\mathcal{I}_4 - \beta\alpha_y) + M_{1,2}\alpha_0 + V_F\hat{k}_x\alpha_x + V_F\left(\frac{x}{\gamma a_B^2} + k_y'\right)\alpha_y + Vk_z\alpha_z \tag{23}$$

and

$$\hat{\mathcal{K}}' = \left[\gamma\left(\beta_y - \beta\beta_0^{(z)}\right)\cos2\phi - \beta_x\sin2\phi\right]k_x - \gamma\left[\beta_x\cos2\phi + \gamma\left(\beta_y - \beta\beta_0^{(z)}\right)\sin2\phi\right]\left(\frac{x}{\gamma a_B^2} + k_y'\right) \tag{24}$$

and

$$\hat{\mathcal{K}}'_t = \beta_x \cos 2\phi + \gamma\left(\beta_y - \beta\beta_0^{(z)}\right)\sin 2\phi. \tag{25}$$

One can see that the Schrödinger equation (22) in the moving reference frame is described by the *effective* magnetic field $\mathcal{B}'$ reduced to $\mathcal{B}' = \mathcal{B}/\gamma$. Although it does not contain the electric field $\mathcal{E}$ explicitly, the terms proportional to β and γ are present in Eq. (22). This means that, in contrast to Dirac fermion, the motion of the Kane fermion in the moving reference frame is still dependent on the frame's velocity defined by the parameter β (cf. Refs. [19,20,23]).

Further, it is convenient to shift the origin of the coordinate x as

$$\tilde{x} = x + \gamma k'_y a_B^2 - \frac{\beta\gamma^2 a_B^2}{V_F}\frac{C_1 + C_2}{2}, \tag{26}$$

which allows Eqs. (22)–(24) to be presented in a more symmetrical form

$$\left[(V_F k'_t + \mathcal{C}\gamma)\begin{pmatrix} \mathcal{I}_4 & -\beta\gamma\,\tan\theta\hat{\mathcal{K}}'_t \\ \beta\gamma\,\tan\theta\hat{\mathcal{K}}'_t & \mathcal{I}_4 \end{pmatrix} + \begin{pmatrix} \tilde{\mathcal{H}}'_1 & V_F\tan\theta\tilde{\mathcal{K}}' \\ -V_F\tan\theta\tilde{\mathcal{K}}' & \tilde{\mathcal{H}}'_2 \end{pmatrix}\right]|\Psi'_{8\times 8}\rangle = 0, \tag{27}$$

where $\mathcal{C} = (C_1 + C_2)/2$ and

$$\tilde{\mathcal{H}}'_{1,2} = \mp\gamma\frac{C_2 - C_1}{2}\mathcal{I}_4 + M_{1,2}\alpha_0 + V_F\hat{k}_x\alpha_x + \frac{V_F}{\gamma a_B^2}\left(\tilde{x} \pm \frac{\beta\gamma^2 a_B^2}{V_F}\frac{C_2 - C_1}{2}\right)\alpha_y + Vk_z\alpha_z \tag{28}$$

and

$$\hat{\mathcal{K}}' = \left[\gamma\left(\beta_y - \beta\beta_0^{(z)}\right)\cos 2\phi - \beta_x \sin 2\phi\right]k_x - \gamma\left[\beta_x\cos 2\phi + \gamma\left(\beta_y - \beta\beta_0^{(z)}\right)\sin 2\phi\right]\frac{\tilde{x}}{\gamma a_B^2}. \tag{29}$$

In Eq. (28), the upper signs correspond to the first Dirac subsystem, while the lower signs are for the second one.

Let us now consider two Dirac subsystems separately. Introducing the ladder operators $a_{1,2}$ and $a^+_{1,2}$

$$a_{1,2} = \frac{1}{\sqrt{2}}\left(\xi \pm \xi_0 + \frac{\partial}{\partial\xi}\right),$$
$$a^+_{1,2} = \frac{1}{\sqrt{2}}\left(\xi \pm \xi_0 - \frac{\partial}{\partial\xi}\right), \tag{30}$$

where

$$\xi = \frac{(1-\beta^2)^{1/4}}{a_B}\tilde{x},$$
$$\xi_0 = \frac{\beta a_B}{V_F(1-\beta^2)^{3/4}}\frac{C_2 - C_1}{2}, \tag{31}$$

each of the Hamiltonians $\tilde{\mathcal{H}}'_{1,2}$ is represented as

$$\tilde{\mathcal{H}}'_{1,2} = \mp\gamma\frac{C_2 - C_1}{2}\mathcal{I}_4 + M_{1,2}\alpha_0 + Vk_z\alpha_z + i\frac{\sqrt{2}V_F(1-\beta^2)^{1/4}}{a_B}\begin{pmatrix} 0 & 0 & 0 & -a_{1,2} \\ 0 & 0 & a^+_{1,2} & 0 \\ 0 & -a_{1,2} & 0 & 0 \\ a^+_{1,2} & 0 & 0 & 0 \end{pmatrix}. \tag{32}$$

This form allows for an exact diagonalization of $\tilde{\mathcal{H}}'_{1,2}$ in terms of harmonic oscillator functions $F_n(\xi \pm \xi_0)$, where the positive and negative sign is respectively associated with the first and second type of the ladder operators. Here, $F_n(\xi) \equiv 0$ if $n < 0$, while for $n \geqslant 0$ it is written as

$$F_n(\xi) = \frac{1}{\sqrt{2^n n!\sqrt{\pi}}}\mathcal{H}_n(\xi)e^{-\frac{\xi^2}{2}}, \tag{33}$$

where $\mathcal{H}_n(\xi)$ are the Hermite polynomials.

In view of the above, the wave function at $\theta = 0$ in Eq. (27) has the form

$$|\Psi'_{8\times 8}\rangle_{\theta=0} = e^{-i\frac{(E'_{\theta=0} - \mathcal{C}\gamma)t'}{\hbar}}e^{ik'_y y'}e^{ik_z z} \times \begin{pmatrix} C_n^{(1)}F_n(\xi + \xi_0) \\ C_n^{(2)}F_{n+1}(\xi + \xi_0) \\ C_n^{(3)}F_n(\xi + \xi_0) \\ C_n^{(4)}F_{n+1}(\xi + \xi_0) \\ C_n^{(5)}F_n(\xi - \xi_0) \\ C_n^{(6)}F_{n+1}(\xi - \xi_0) \\ C_n^{(7)}F_n(\xi - \xi_0) \\ C_n^{(8)}F_{n+1}(\xi - \xi_0) \end{pmatrix}, \tag{34}$$

where n is Landau level index, $C_n^{(l)}$ $(l = 1 \ldots 8)$ are the constants, and

$$E'_{\theta=0} = \mp\gamma\frac{C_2 - C_1}{2} + \tau\sqrt{M_{1,2}^2 + V^2k_z^2 + \frac{2V^2(n+1)}{\gamma a_B^2}}, \tag{35}$$

with $\tau = +1$ and $\tau = -1$ for conduction and valence bands, respectively.

Now let us return to the more general case of Eq. (27) with nonzero θ. Since the time-momentum operator k'_t commutes with the Hamiltonian in Eq. (27), the wave function is presented in the similar form $|\Psi'_{8\times 8}\rangle = \exp[-i(E' - \mathcal{C}\gamma)t'/\hbar]|\Phi'_{8\times 8}\rangle$, where $|\Phi'_{8\times 8}\rangle$ is independent of t' and obeys the equation

$$\begin{pmatrix} \tilde{\mathcal{H}}'_1 & V_F\tan\theta\tilde{\mathcal{K}}' \\ -V_F\tan\theta\tilde{\mathcal{K}}' & \tilde{\mathcal{H}}'_2 \end{pmatrix}|\Phi'_{8\times 8}\rangle = E'\begin{pmatrix} \mathcal{I}_4 & -\beta\gamma\,\tan\theta\hat{\mathcal{K}}'_t \\ \beta\gamma\,\tan\theta\hat{\mathcal{K}}'_t & \mathcal{I}_4 \end{pmatrix}|\Phi'_{8\times 8}\rangle. \tag{36}$$

As seen, Eq. (36) differs from a conventional eigenvalue problem due to the matrix coefficient at the energy E'. Since such matrix does not commute with the matrix in the left side and the inverse matrix has a singularity at $\beta < 1$, Eq. (36)

cannot be represented in the form of the eigenvalue problem. A similar type of mathematical problem has recently been considered in the context of Dirac systems [40].

In order to find the solution of Eq. (36), the function $|\Phi'_{8\times 8}\rangle$ is convenient to expand in the complete basis of the wave functions in Eq. (34) found at $\theta = 0$:

$$|\Phi'_{8\times 8}\rangle = e^{ik'_y y'} e^{ik_z z} \sum_{n=-1}^{\infty} \begin{pmatrix} C_n^{(1)} F_n(\xi+\xi_0) \\ C_n^{(2)} F_{n+1}(\xi+\xi_0) \\ C_n^{(3)} F_n(\xi+\xi_0) \\ C_n^{(4)} F_{n+1}(\xi+\xi_0) \\ C_n^{(5)} F_n(\xi-\xi_0) \\ C_n^{(6)} F_{n+1}(\xi-\xi_0) \\ C_n^{(7)} F_n(\xi-\xi_0) \\ C_n^{(8)} F_{n+1}(\xi-\xi_0) \end{pmatrix}. \tag{37}$$

Note that n ceases to be a good quantum number in contrast to the case of $\theta = 0$.

The present expansion leads to a matrix representation of Eq. (36), where the energies and vectors $\hat{C}_n = (C_n^{(1)}, \ldots, C_n^{(8)})^T$ are found from the secular equation:

$$\sum_{n=-1}^{\infty} (\hat{\mathcal{H}}'_{mn} + E'\hat{\mathcal{A}}'_{mn})\hat{C}_n = E'\hat{C}_m, \tag{38}$$

where $\hat{\mathcal{H}}'_{nm}$ and $\hat{\mathcal{A}}'_{mn}$ are 8×8 matrices written in the block form as

$$\hat{\mathcal{H}}'_{mn} = \begin{pmatrix} \hat{\mathcal{U}}^{(1)}_{mn} & V\ \sin\theta\hat{\mathcal{R}}_{mn}(\xi_0, -\xi_0) \\ V\ \sin\theta\hat{\mathcal{R}}_{mn}(-\xi_0, \xi_0) & \hat{\mathcal{U}}^{(2)}_{mn} \end{pmatrix} \tag{39}$$

and

$$\hat{\mathcal{A}}'_{mn} = \beta\gamma\ \tan\theta \begin{pmatrix} 0 & \hat{\mathcal{T}}_{mn}(\xi_0, -\xi_0) \\ -\hat{\mathcal{T}}_{mn}(-\xi_0, \xi_0) & 0 \end{pmatrix}. \tag{40}$$

Here, $\hat{\mathcal{U}}^{(1,2)}_{mn}$ represent the expansion of the Dirac blocks $\tilde{\mathcal{H}}'_{1,2}$, while $\hat{\mathcal{R}}_{mn}(\pm\xi_0, \mp\xi_0)$ and $\hat{\mathcal{T}}_{mn}(\pm\xi_0, \mp\xi_0)$ arise due to the antidiagonal blocks in Eq. (36).

Note that all matrix elements of $\hat{\mathcal{H}}'_{mn}$ and $\hat{\mathcal{A}}'_{mn}$ in Eq. (38) are calculated analytically. Particularly, $\hat{\mathcal{U}}^{(1,2)}_{mn}$ are written as follows:

$$\hat{\mathcal{U}}^{(1,2)}_{mn} = \begin{pmatrix} M^{(\mp)}_{1,2}\mathcal{F}_m\mathcal{F}_n & 0 & Vk_z\mathcal{F}_m\mathcal{F}_n & 0 \\ 0 & M^{(\mp)}_{1,2}\mathcal{F}_{m+1}\mathcal{F}_{n+1} & 0 & -Vk_z\mathcal{F}_{m+1}\mathcal{F}_{n+1} \\ Vk_z\mathcal{F}_m\mathcal{F}_n & 0 & -M^{(\pm)}_{1,2}\mathcal{F}_m\mathcal{F}_n & 0 \\ 0 & -Vk_z\mathcal{F}_{m+1}\mathcal{F}_{n+1} & 0 & -M^{(\pm)}_{1,2}\mathcal{F}_{m+1}\mathcal{F}_{n+1} \end{pmatrix}\delta_{m,n}$$
$$+ i\frac{\sqrt{2}V_F(1-\beta^2)^{1/4}}{a_B} \begin{pmatrix} 0 & 0 & 0 & -\sqrt{n+1}\mathcal{F}_m\mathcal{F}_{n+1} \\ 0 & 0 & \sqrt{n+1}\mathcal{F}_{m+1}\mathcal{F}_n & 0 \\ 0 & -\sqrt{n+1}\mathcal{F}_m\mathcal{F}_{n+1} & 0 & 0 \\ \sqrt{n+1}\mathcal{F}_{m+1}\mathcal{F}_n & 0 & 0 & 0 \end{pmatrix}\delta_{m,n}, \tag{41}$$

where $M^{(\pm)}_{1,2} = M_{1,2} \pm \gamma(C_2 - C_1)/2$; $\delta_{m,n}$ is the Kronecker delta, while $\mathcal{F}_n = 1$ for $n \geqslant 0$ and $\mathcal{F}_n = 0$ for negative n values. In Eq. (41), the upper and lower signs correspond to $\hat{\mathcal{U}}^{(1)}_{mn}$ and $\hat{\mathcal{U}}^{(2)}_{mn}$, respectively.

The matrices $\hat{\mathcal{R}}_{mn}(\pm\xi_0, \mp\xi_0)$ are rather cumbersome and not presented here. Their calculation is carried out in a trivial way, if one expresses $\tilde{\mathcal{K}}'$ in Eq. (29) either through the operators a_1, a_1^+ or a_2, a_2^+:

$$\sqrt{\gamma}a_B\hat{\mathcal{K}}' = \pm\gamma\left[\beta_x\cos 2\phi + \gamma\left(\beta_y - \beta\beta_0^{(z)}\right)\sin 2\phi\right]\xi_0$$
$$- \gamma\left[\beta_x\cos 2\phi + \gamma\left(\beta_y - \beta\beta_0^{(z)}\right)\sin 2\phi\right]\frac{a^+_{1,2} + a_{1,2}}{\sqrt{2}}$$
$$+ i\left[\gamma\left(\beta_y - \beta\beta_0^{(z)}\right)\cos 2\phi - \beta_x\sin 2\phi\right]\frac{a^+_{1,2} - a_{1,2}}{\sqrt{2}},$$

depending on whether the functions $F_n(\xi+\xi_0)$ or $F_n(\xi-\xi_0)$ appear on the left, respectively.

As a result, after the integration, in addition to the factors $\mathcal{F}_{n_1}$ and $\mathcal{F}_{n_2}$, *all of the matrix elements* of $\hat{\mathcal{R}}_{mn}(\pm\xi_0, \mp\xi_0)$ will contain a factor $\Gamma_{n_1,n_2}(\xi_0, -\xi_0)$ [instead of the Kronecker delta in Eq. (41)] defined as

$$\Gamma_{n_1,n_2}(\xi_1, \xi_2) = \int_{-\infty}^{+\infty} F_{n_1}(\xi+\xi_1)F_{n_2}(\xi+\xi_2)d\xi$$
$$= \sqrt{\frac{2^{n-m}}{(n-m)!}}e^{-\delta^2}\mathcal{L}_m^{n-m}(2\delta^2)$$
$$\times \begin{cases} \left(\dfrac{\xi_1-\xi_2}{2}\right)^{n_1-n_2}, & n_1 \geqslant n_2, \\ \left(\dfrac{\xi_2-\xi_1}{2}\right)^{n_2-n_1}, & n_1 < n_2, \end{cases} \tag{42}$$

where $n = \max(n_1, n_2)$, $m = \min(n_1, n_2)$, and $\delta = (\xi_2 - \xi_1)/2$ [41].

The similar Γ factors also arise in the calculations of the matrix elements of $\hat{\mathcal{A}}'_{mn}$. By introducing $a_{n_1,n_2}(\xi_1, \xi_2) = \Gamma_{n_1,n_2}(\xi_1, \xi_2)\mathcal{F}_{n_1}\mathcal{F}_{n_2}$, one can write $\hat{\mathcal{T}}_{mn}(\xi_1, \xi_2)$ in Eq. (40) as follows:

$$\hat{\mathcal{T}}_{mn}(\xi_1,\xi_2) = i\begin{pmatrix} -\beta a_{m,n}(\xi_1,\xi_2)\sin 2\phi & 0 & 0 & -a_{m,n+1}(\xi_1,\xi_2)e^{2i\phi} \\ 0 & \beta a_{m+1,n+1}(\xi_1,\xi_2)\sin 2\phi & a_{m+1,n}(\xi_1,\xi_2)e^{-2i\phi} & 0 \\ 0 & a_{m,n+1}(\xi_1,\xi_2)e^{2i\phi} & \beta a_{m,n}(\xi_1,\xi_2)\sin 2\phi & 0 \\ -a_{m+1,n}(\xi_1,\xi_2)e^{-2i\phi} & 0 & 0 & -\beta a_{m+1,n+1}(\xi_1,\xi_2)\sin 2\phi \end{pmatrix}. \quad (43)$$

Thus, using Eqs. (39)–(43), the solution of the Schrödinger equation in the boosted frame is reduced to the algebraic secular equation in Eq. (38). The secular equation was solved by an iterative method, the i step of which was reduced to the eigenvalue problem for the matrix with the energy E'_{i-1} found at the previous iteration:

$$\sum_{n=-1}^{N}(\hat{\mathcal{H}}'_{mn} + E'_{(i-1)}\hat{\mathcal{A}}'_{mn})\hat{\mathcal{C}}_n = E'_{(i)}\hat{\mathcal{C}}_m.$$

The energy $E'_{(0)}$ for the zeroth iteration has been reduced to zero. Note that the solution of the eigenvalue problem at each iteration can be performed with any required accuracy by using the correspondingly truncated matrix based on the large number N of terms involved in the expansion of $|\Phi'_{8\times 8}\rangle$ in Eq. (39). In Sec. IV, we present the calculations performed for $N = 50$ with the five iteration steps.

Knowing the energies E' and wave functions $|\Psi'_{8\times 8}\rangle$ in the boosted frame, the "physical" energies E and wave function $|\Psi_{8\times 8}\rangle$ in Eq. (19) are found by means of the inverse boost transformation

$$E = \frac{C_1 + C_2}{2} + E'\sqrt{1-\beta^2} - \beta V k_y \cos\theta, \quad (44)$$

$$|\Psi_{8\times 8}\rangle \propto e^{-i\frac{Et}{\hbar}} e^{ik_y y} e^{ik_z z}\hat{\mathbb{A}} \sum_{n=-1}^{\infty}\begin{pmatrix} C_n^{(1)}F_n(\xi+\xi_0) \\ C_n^{(2)}F_{n+1}(\xi+\xi_0) \\ C_n^{(3)}F_n(\xi+\xi_0) \\ C_n^{(4)}F_{n+1}(\xi+\xi_0) \\ C_n^{(5)}F_n(\xi-\xi_0) \\ C_n^{(6)}F_{n+1}(\xi-\xi_0) \\ C_n^{(7)}F_n(\xi-\xi_0) \\ C_n^{(8)}F_{n+1}(\xi-\xi_0) \end{pmatrix}, \quad (45)$$

$$\xi = \frac{(1-\beta^2)^{1/4}}{a_B}\left(x + \frac{a_B^2 k_y}{1-\beta^2} + \frac{\beta a_B^2}{1-\beta^2}\frac{E - C_1 - C_2}{V\cos\theta}\right),$$

$$\xi_0 = \frac{(1-\beta^2)^{1/4}}{a_B}\left(\frac{\beta a_B^2}{1-\beta^2}\frac{C_2 - C_1}{2V\cos\theta}\right), \quad (46)$$

where $\hat{\mathbb{A}} = \sigma_0 \otimes \exp(-\alpha_y \cdot \alpha/2)$. Note that, in the above equations, $\beta = (c\hbar\mathcal{E})/(V\mathcal{B}\cos\theta)$, while α is defined by Eq. (21). In the absence of electric field ($\beta = 0$), the formulas above are reduced to the results of conventional Landau level calculations on the basis of the nonisotropic Hamiltonian in Eq. (18).

B. $\mathcal{E} \parallel$ [100] and $\mathcal{B} \parallel$ [010]

Let us now consider another orientation of the electric and magnetic fields. Assuming $x \parallel [100]$, $y \parallel [00\bar{1}]$, and $z \parallel [010]$, and introducing additional β matrices as

$$\beta_z = \begin{pmatrix} 0 & \sigma_z \\ -\sigma_z & 0 \end{pmatrix}, \quad \beta_x^{(0)} = \begin{pmatrix} i\sigma_x & 0 \\ 0 & -i\sigma_x \end{pmatrix}, \quad (47)$$

the (3+1)-band Hamiltonian has the form

$$\hat{\mathcal{H}}_{8\times 8}^{(3+1)}(\mathbf{k}) = \begin{pmatrix} \hat{\mathcal{H}}_D^{(1)}(\mathbf{k}) & V\sin\theta\hat{\mathcal{K}}(\mathbf{k}) \\ -V\sin\theta\hat{\mathcal{K}}(\mathbf{k}) & \hat{\mathcal{H}}_D^{(2)}(\mathbf{k}) \end{pmatrix}, \quad (48)$$

where $\hat{\mathcal{H}}_D^{(1,2)}(\mathbf{k})$ and $\hat{\mathcal{K}}(\mathbf{k})$ are written as

$$\hat{\mathcal{H}}_D^{(1,2)}(\mathbf{k}) = C_{1,2}\mathcal{I}_4 + M_{1,2}\alpha_0 + V\cos\theta k_x\alpha_x + Vk_y\alpha_y + V\cos\theta k_z\alpha_z \quad (49)$$

and

$$\hat{\mathcal{K}}(\mathbf{k}) = k_x\beta_y - k_z\beta_z. \quad (50)$$

Assuming the orientation of electric field $\mathcal{E}$ along the x axis and magnetic field $\mathcal{B}$ along the z axis and simultaneously making the Peierls substitution presented by Eq. (18), we arrive at an equation similar to Eq. (19). Then, after the Lorentz boost in the y direction [see Eq. (20)] with the parameter α defined as

$$\tanh\alpha = -\delta = -\frac{c\hbar}{V}\frac{\mathcal{E}}{\mathcal{B}}, \quad \cosh\alpha = \tilde{\gamma} = \frac{1}{\sqrt{1-\delta^2}}, \quad (51)$$

the Schrödinger equation in the moving frame of reference is rewritten as

$$\left[\begin{pmatrix} \hat{\mathcal{H}}'_1 & V\sin\theta\hat{\mathcal{K}}' \\ -V\sin\theta\hat{\mathcal{K}}' & \hat{\mathcal{H}}'_2 \end{pmatrix} + Vk'_t\mathcal{I}_8\right]|\Psi'_{8\times 8}\rangle = 0, \quad (52)$$

where $k'_t = -i\hbar\partial/\partial(Vt')$ is the time-momentum operator, $\hat{\mathcal{H}}'_{1,2}$ are the boosted Dirac Hamiltonians

$$\hat{\mathcal{H}}'_{1,2} = \tilde{\gamma}C_{1,2}(\mathcal{I}_4 - \delta\alpha_y) + M_{1,2}\alpha_0 + V\cos\theta\hat{k}_x\alpha_x + V\left(\frac{x}{\tilde{\gamma}a_B^2} + k'_y\right)\alpha_y + V\cos\theta k_z\alpha_z, \quad (53)$$

and

$$\hat{\mathcal{K}}' = \tilde{\gamma}\left(\beta_y - \delta\beta_0^{(z)}\right)k_x - \tilde{\gamma}\left(\beta_z + \delta\beta_0^{(x)}\right)k_z. \quad (54)$$

As seen from Eq. (53), in the moving frame of reference the effective magnetic field $\mathcal{B}'$ is reduced as $\mathcal{B}' = \mathcal{B}/\tilde{\gamma}$ [cf. Eqs. (23) and (24) in Sec. III A]. Similar to the case of $\mathcal{B} \parallel [010]$ considered previously, the Schrödinger equation for the Kane fermion in the moving reference frame contains additional terms related to the frame's velocity defined by parameter δ.

By analogy with Eq. (26), it is also convenient here to shift the origin of the coordinate x as

$$\tilde{x} = x + \tilde{\gamma} k_y' a_B^2 - \frac{\delta \tilde{\gamma}^2 a_B^2}{V} \frac{C_1 + C_2}{2}. \tag{55}$$

The latter allows us to rewrite Eqs. (52)–(54) in the form

$$\left[\begin{pmatrix} \tilde{\mathcal{H}}_1' & V \sin\theta \hat{\mathcal{K}}' \\ -V \sin\theta \hat{\mathcal{K}}' & \tilde{\mathcal{H}}_2' \end{pmatrix} + (V k_t' + \mathcal{C}\tilde{\gamma}) \mathcal{I}_8 \right] |\Psi_{8\times 8}'\rangle = 0, \tag{56}$$

where $\mathcal{C} = (C_1 + C_2)/2$ and

$$\tilde{\mathcal{H}}_{1,2}' = \mp\tilde{\gamma} \frac{C_2 - C_1}{2} \mathcal{I}_4 + M_{1,2}\alpha_0 + V \cos\theta \hat{k}_x \alpha_x + \frac{V}{\tilde{\gamma} a_B^2} \left(\tilde{x} \pm \frac{\delta \tilde{\gamma}^2 a_B^2}{V} \frac{C_2 - C_1}{2} \right) \alpha_y + V \cos\theta k_z \alpha_z. \tag{57}$$

Here, the upper signs correspond to the first Dirac subsystem, while the lower signs are for the second one. Note that the origin changing does not affect the form of the antidiagonal blocks $\hat{\mathcal{K}}'$ in Eq. (57).

Introducing the ladder operators $b_{1,2}$ and $b_{1,2}^+$

$$b_{1,2} = \frac{1}{\sqrt{2}} \left(\xi \pm \xi_0 + \frac{\partial}{\partial \xi} \right),$$
$$b_{1,2}^+ = \frac{1}{\sqrt{2}} \left(\xi \pm \xi_0 - \frac{\partial}{\partial \xi} \right), \tag{58}$$

where

$$\xi = \frac{(1-\delta^2)^{1/4}}{a_B \sqrt{\cos\theta}} \tilde{x},$$
$$\xi_0 = \frac{\delta a_B}{V \sqrt{\cos\theta} (1-\delta^2)^{3/4}} \frac{C_2 - C_1}{2}, \tag{59}$$

each of the Hamiltonians $\tilde{\mathcal{H}}_{1,2}'$ and $\hat{\mathcal{K}}'$ in Eq. (56) are represented as

$$\tilde{\mathcal{H}}_{1,2}' = \mp\tilde{\gamma} \frac{C_2 - C_1}{2} \mathcal{I}_4 + M_{1,2}\alpha_0 + V \cos\theta k_z \alpha_z + i \frac{\sqrt{2} V \sqrt{\cos\theta} (1-\delta^2)^{1/4}}{a_B} \begin{pmatrix} 0 & 0 & 0 & -b_{1,2} \\ 0 & 0 & b_{1,2}^+ & 0 \\ 0 & -b_{1,2} & 0 & 0 \\ b_{1,2}^+ & 0 & 0 & 0 \end{pmatrix} \tag{60}$$

and

$$\hat{\mathcal{K}}' = i\tilde{\gamma} \left(\beta_y - \delta \beta_0^{(z)} \right) \frac{(1-\delta^2)^{1/4}}{a_B \sqrt{\cos\theta}} \frac{b_{1,2}^+ - b_{1,2}}{\sqrt{2}} - \tilde{\gamma} \left(\beta_z + \delta \beta_0^{(x)} \right) k_z. \tag{61}$$

Then, representing the wave function in the form $|\Psi_{8\times 8}'\rangle = \exp[-i(E' - \mathcal{C}\gamma)t'/\hbar] |\Phi_{8\times 8}'\rangle$ and using the basis expansion of Eq. (37) but with ξ and ξ_0 defined above, the Schrödinger equation (56) in the moving reference frame is reduced to the eigenvalue problem [cf. Eq. (38)]:

$$\sum_{n=-1}^{\infty} \hat{\mathcal{H}}_{mn}' \hat{\mathcal{C}}_n = E' \hat{\mathcal{C}}_m, \tag{62}$$

where $\hat{\mathcal{H}}_{nm}'$ is an 8×8 matrix written as follows:

$$\hat{\mathcal{H}}_{mn}' = \begin{pmatrix} \hat{\mathcal{U}}_{mn}^{(1)} & V \sin\theta \hat{\mathcal{R}}_{mn}(\xi_0, -\xi_0) \\ V \sin\theta \hat{\mathcal{R}}_{mn}(-\xi_0, \xi_0) & \hat{\mathcal{U}}_{mn}^{(2)} \end{pmatrix}, \tag{63}$$

where $\hat{\mathcal{U}}_{mn}^{(1,2)}$ represent the expansion of $\tilde{\mathcal{H}}_{1,2}'$ in Eq. (60), while $\hat{\mathcal{R}}_{mn}(\pm\xi_0, \mp\xi_0)$ results from the antidiagonal blocks $\hat{\mathcal{K}}'$ in Eq. (61). In this section, we omit explicit expressions for $\hat{\mathcal{U}}_{mn}^{(1,2)}$ and $\hat{\mathcal{R}}_{mn}(\pm\xi_0, \mp\xi_0)$, which are not difficult to obtain. Note that $\hat{\mathcal{U}}_{mn}^{(1,2)}$ are proportional to the Kronecker delta $\delta_{m,n}$ [cf. Eq. (41)], while all the matrix elements of $\hat{\mathcal{R}}_{mn}(\pm\xi_0, \mp\xi_0)$ contain the Γ factors introduced by Eq. (42).

In the absence of nondiagonal blocks in Eq. (63), the eigenvalue problem in Eq. (62) can be analytically solved, resulting in

$$E_{\theta=0}' = \mp\tilde{\gamma} \frac{C_2 - C_1}{2} + \tau \sqrt{M_{1,2}^2 + V^2 k_z^2 + \frac{2V^2(n+1)}{\tilde{\gamma} a_B^2}}, \tag{64}$$

where n is the Landau level index; $\tau = +1$ and $\tau = -1$ for conduction and valence bands, respectively. At nonzero θ, that solution of the eigenvalue problem can be obtained by numerical calculation with any required accuracy.

After knowing the energies E' and wave functions $|\Psi_{8\times 8}'\rangle$ in the boosted frame, the energies E and wave function $|\Psi_{8\times 8}\rangle$ of the (3+1)-band Hamiltonian in Eq. (48) are found by means of the inverse boost transformation

$$E = \frac{C_1 + C_2}{2} + E' \sqrt{1 - \delta^2} - \delta V k_y, \tag{65}$$

$$|\Psi_{8\times 8}\rangle \propto e^{-i\frac{Et}{\hbar}} e^{ik_y y} e^{ik_z z} \hat{\mathbb{A}} \sum_{n=-1}^{\infty} \begin{pmatrix} C_n^{(1)} F_n(\xi + \xi_0) \\ C_n^{(2)} F_{n+1}(\xi + \xi_0) \\ C_n^{(3)} F_n(\xi + \xi_0) \\ C_n^{(4)} F_{n+1}(\xi + \xi_0) \\ C_n^{(5)} F_n(\xi - \xi_0) \\ C_n^{(6)} F_{n+1}(\xi - \xi_0) \\ C_n^{(7)} F_n(\xi - \xi_0) \\ C_n^{(8)} F_{n+1}(\xi - \xi_0) \end{pmatrix}, \tag{66}$$

$$\xi = \frac{(1-\delta^2)^{1/4}}{a_B \sqrt{\cos\theta}} \left(x + \frac{a_B^2 k_y}{1-\delta^2} + \frac{\delta a_B^2}{1-\delta^2} \frac{E - C_1 - C_2}{V} \right),$$
$$\xi_0 = \frac{(1-\delta^2)^{1/4}}{a_B \sqrt{\cos\theta}} \left(\frac{\delta a_B^2}{1-\delta^2} \frac{C_2 - C_1}{2V} \right), \tag{67}$$

where $\hat{\mathbb{A}} = \sigma_0 \otimes \exp(-\alpha_y \cdot \alpha/2)$. We recall that in the above equations, $\delta = (c\hbar\mathcal{E})/(V\mathcal{B})$, while α is defined by Eq. (51).

IV. RESULTS AND DISCUSSION

Let us now discuss some properties of Kane fermions directly seen from the (3+1)-band Hamiltonian in crossed electric and magnetic fields. First, the structure of the (3+1)-band Hamiltonian proves the origin of the Kane fermions in HgCdTe as spin-1/2 particles. In this sense, the Kane fermion should be considered as a superposition of two Dirac particles of different masses hybridized in a special way. Interestingly, this situation is partially reminiscent of the case of the Dirac fermion itself, which is also a superposition of two Weyl

particles mutually hybridized due to a finite rest mass. Note that the (3+1)-band representation of the Kane fermion is retained for any position of the Γ_{7c}, Γ_{6c}, and Γ_{8v} bands [see Eq. (13)]; therefore, it describes HgCdTe crystals with inverted and noninverted band structures, as well as for Cd_3As_2 [42].

As first shown by Aronov and Pikus [19,20], the pseudorelativistic character of Dirac fermions in semiconductors allows us to apply the Lorentz boost to eliminate the electric field $\mathcal{E}'$ from the Hamiltonian in the reference frame moving with the drift velocity $V_d = c\mathcal{E}/\mathcal{B}$. Thus the Dirac Hamiltonian in the moving frame includes only the effective magnetic field $\mathcal{B}' = \mathcal{B}\sqrt{1-\delta^2}$, where δ is the ratio of V_d to the effective speed of the light $\tilde{c} = V/\hbar$. Note that such an interpretation is compatible with the Lorentz transformation for electric and magnetic fields also described by the effective speed of the light. Indeed, in the frame moving with velocity $\mathbf{V}$, the electric $\mathcal{E}$ and magnetic $\mathcal{B}$ fields formally transform according to

$$\mathcal{E}' = \gamma_L\left(\mathcal{E} + \frac{1}{c_L}\mathbf{V}\times\mathcal{B}\right) - \frac{\gamma_L^2}{\gamma_L+1}\frac{\mathbf{V}(\mathbf{V}\cdot\mathcal{E})}{c_L^2},$$
$$\mathcal{B}' = \gamma_L\left(\mathcal{B} - \frac{1}{c_L}\mathbf{V}\times\mathcal{E}\right) - \frac{\gamma_L^2}{\gamma_L+1}\frac{\mathbf{V}(\mathbf{V}\cdot\mathcal{B})}{c_L^2}, \qquad (68)$$

where c_L and γ_L are related as $\gamma_L = 1/\sqrt{1-|\mathbf{V}|^2/c_L^2}$. It can be seen that this transformation leaves invariant the quantities

$$\mathcal{B}'^2 - \mathcal{E}'^2 = \mathcal{B}^2 - \mathcal{E}^2, \quad (\mathcal{B}'\cdot\mathcal{E}') = (\mathcal{B}\cdot\mathcal{E}), \qquad (69)$$

for *any values* of c_L. If $\mathcal{B}\perp\mathcal{E}$ and $\mathcal{B} > \mathcal{E}$ one can always eliminate the electric field by choosing a suitable moving coordinate system. For Dirac fermions, the transformations of the Hamiltonian and fields become compatible only if $c_L = \tilde{c}$.

For Kane fermions, the effective magnetic field $\mathcal{B}'$ in the moving frame, in which $\mathcal{E}' = 0$, depends on the orientations of $\mathcal{E}$ and $\mathcal{B}$ with respect to the main crystallographic axes. Therefore, a compatibility of the (3+1)-band Hamiltonian with the fields' transformation in Eq. (69) takes place at the values of c_L dependent on the crystallographic orientations of $\mathcal{E}$ and $\mathcal{B}$ in the original frame as well (see Appendix C). Particularly, for the two cases considered in Sec. III, $c_L = \tilde{c}\cos\theta$ for $\mathcal{B}\parallel[001]$, while, for $\mathcal{B}\parallel[001]$ and $\mathcal{E}\parallel[100]$, $c_L = \tilde{c}$.

Another difference between Kane fermions and Dirac particles is the breaking of spherical symmetry, which is a consequence of the symmetry of zinc-blende crystals. The latter results in the fact that the Landau level index, defined by the corresponding harmonic oscillator function in Eq. (33), ceases to be a good quantum number that complicates the Landau level fan calculated within the (3+1)-band model. Figure 2 provides the energies of Landau levels for HgCdTe bulk crystals with inverted and noninverted band structures in the absence of electric field ($\beta = 0$) when magnetic field $\mathcal{B}$ is oriented along the [001] crystallographic axis. In order to solve the eigenvalue problem arising from the secular equation (38) at $\beta = 0$, we have used the truncated matrix composed of $\hat{\mathcal{H}}'_{mn}$ with $N = 50$ terms in the expansion of $|\Phi'_{8\times8}\rangle$ in Eq. (39). It is seen that, although the Landau levels for the light-hole and Γ_{6c} bands are in good agreement with Eq. (5), the nonzero curvature of the heavy hole band in the absence of rotational symmetry in the plane perpendicular to the magnetic field leads to a nonequidistant spectrum of the Landau levels. Note that $\theta = \pi/3$ for zinc-blende HgCdTe and Cd_3As_2 crystals.

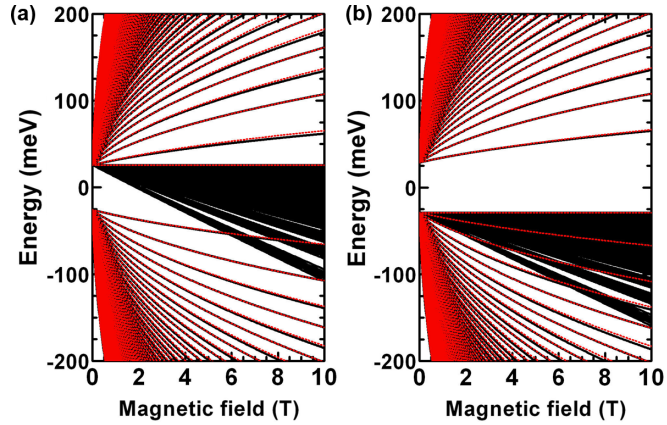

FIG. 2. Landau levels in the absence of electric field in (a) $Hg_{0.14}Cd_{0.86}Te$ and (b) $Hg_{0.20}Cd_{0.80}Te$ bulk crystals with inverted and noninverted band structures, respectively (cf. Fig. 1). The solid black curves are the calculations within the (3+1)-band model, while the dotted red curves represent the calculations based on Eq. (5). For both cases, $\mathcal{B}\parallel[001]$. The second conduction Γ_{7c} band is high in energy lying beyond the figure scale.

In the presence of electric field $\mathcal{E}$, the cubic symmetry leads to a strong dependence of the energy and the collapse of the Landau levels on the orientation of electric and magnetic field relative to the main axes of the crystal. This is well illustrated by the two cases considered in Sec. III, in which the collapse occurs when the drift velocity V_d reaches $V\cos\theta/\hbar$ for $\mathcal{B}\parallel[001]$ and $V/\hbar$ for $\mathcal{B}\parallel[010]$, $\mathcal{E}\parallel[100]$. The former corresponds to only *half* of the effective speed of the light $\tilde{c} = V/\hbar$, since $\theta = \pi/3$ for the Kane fermions. It can be shown that, for an arbitrary orientation of the magnetic field (and the electric field $\mathcal{E}\perp\mathcal{B}$), the Landau levels collapse when V_d is equal to V_d^* lying between *half* and *whole* values of $V/\hbar$ (see Appendix C).

Let us now take a closer look at the Landau level evolution in crossed electric and magnetic fields. As shown in Sec. III, in the presence of $\mathcal{E}$, the energies of Landau levels of Kane fermions are connected with the energies E' and wave functions $|\Psi'_{8\times8}\rangle$ of the boosted (3+1)-band Hamiltonian. The calculations in the moving frame, in their turn, are reduced to the solution of secular equations in the given expansion basis [see Eqs. (38) and (62)] composed of 4×4 matrices describing the two Dirac subsystems. The two diagonal matrices in Eqs. (39) and (63), namely $\hat{\mathcal{U}}^{(1,2)}_{mn}$, describe the evolution of each of the Dirac subsystems, while the antidiagonal matrices $\hat{\mathcal{R}}_{mn}(\pm\xi_0,\mp\xi_0)$ [as well as $\hat{\mathcal{T}}_{mn}(\pm\xi_0,\mp\xi_0)$ in Eq. (40)] represent the mutual hybridization between the subsystems.

The most important point of the secular equations (38) and (62) is that each of the matrix elements of $\hat{\mathcal{R}}_{mn}(\pm\xi_0,\mp\xi_0)$ and $\hat{\mathcal{T}}_{mn}(\pm\xi_0,\mp\xi_0)$ contains the corresponding Γ factor. As seen from Eq. (43), $\Gamma_{n_1,n_2}(\pm\xi_0,\mp\xi_0)$ is proportional to the Gaussian factor $\exp(-\xi_0^2)$ at any values of n_1 and n_2. The latter makes it possible to immediately understand the behavior of Landau levels in strong electric fields.

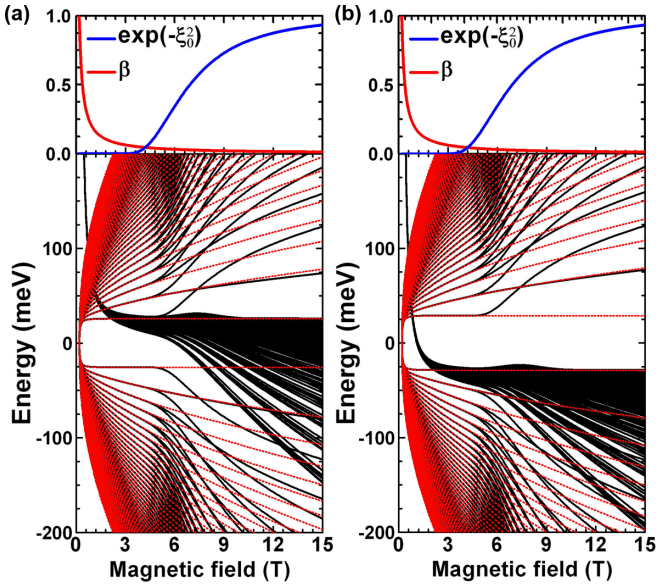

FIG. 3. Landau levels at $\mathcal{E} = 1000$ V/cm and $k_y = k_z = 0$ in (a) $Hg_{0.14}Cd_{0.86}Te$ and (b) $Hg_{0.20}Cd_{0.80}Te$ bulk crystals for $\mathcal{B} \parallel [001]$ and $\mathcal{E} \parallel [100]$. The solid black curves are the calculations within the (3+1)-band model (see Sec. III A), while the dotted red curves represent the calculations based on Eq. (71). Here, the critical magnetic field $B_c = (c\hbar\mathcal{E})/(V\cos\theta)$, at which Landau levels of Kane fermions ($\theta = \pi/3$) collapse, approximately equals 0.19 T. The upper panels represent β and $e^{-\xi_0^2}$ [where β and ξ_0 are defined by Eq. (21) and Eq. (31), respectively] as functions of magnetic field.

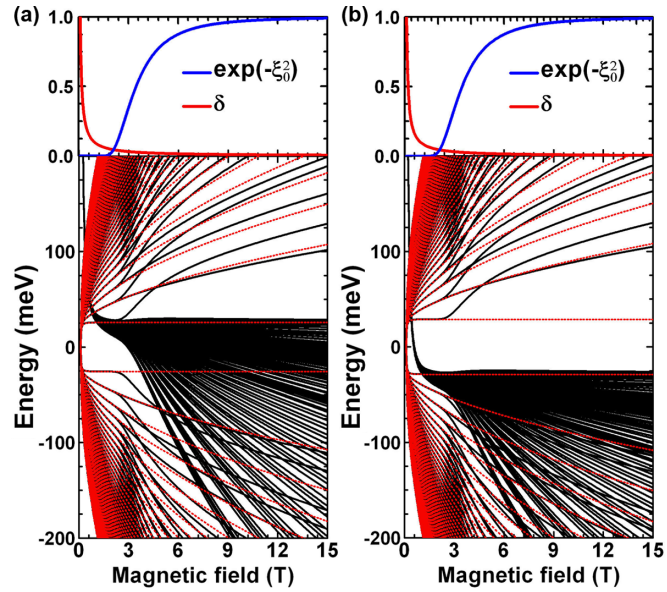

FIG. 4. Landau levels at $\mathcal{E} = 1000$ V/cm and $k_y = k_z = 0$ in (a) $Hg_{0.14}Cd_{0.86}Te$ and (b) $Hg_{0.20}Cd_{0.80}Te$ bulk crystals for $\mathcal{B} \parallel [010]$ and $\mathcal{E} \parallel [100]$. The solid black curves are the calculations within the (3+1)-band model (see Sec. III B), while the dotted red curves represent the calculations based on Eq. (73). Here, the critical magnetic field $B_c = c\hbar\mathcal{E}/V$, at which Landau levels of Kane fermions ($\theta = \pi/3$) collapse, approximately equals 0.095 T. The upper panels represent δ and $e^{-\xi_0^2}$ [where δ and ξ_0 are defined by Eq. (51) and Eq. (59), respectively] as functions of magnetic field.

Particularly, for the case of $\mathcal{B} \parallel [001]$ (see Sec. III A), the antidiagonal blocks of $\hat{\mathcal{H}}'_{mn}$ in Eq. (39) and $\hat{\mathcal{T}}_{mn}(\pm\xi_0, \mp\xi_0)$ in Eq. (40) vanish at $\beta \to 1$ due to $\xi_0 \to \infty$ and

$$e^{-\xi_0^2} = \exp\left[-\frac{\beta^2 a_B^2 (C_2 - C_1)^2}{4V^2 \cos^2\theta (1-\beta^2)^{3/2}}\right] \to 0 \qquad (70)$$

if $C_1 \neq C_2$, which is always the case of HgCdTe and Cd_3As_2 [42] crystals. Since the Gaussian function $e^{-\xi_0^2}$ falls off very quickly, the antidiagonal blocks $\hat{\mathcal{R}}_{mn}(\pm\xi_0, \mp\xi_0)$ and $\hat{\mathcal{T}}_{mn}(\pm\xi_0, \mp\xi_0)$ become negligibly small long before β reaches 1. In this case, the inverse Lorentz transformation gives the following Landau level energies:

$$E_{\text{Dirac}}^{[001]} = C_{1,2} - \beta V k_y \cos\theta \pm \sqrt{1-\beta^2} \times \sqrt{M_{1,2}^2 + V^2 k_z^2 + \sqrt{1-\beta^2}\frac{2V^2(n+1)\cos^2\theta}{a_B^2}}, \qquad (71)$$

where $n \geqslant -1$ and $\beta = \hbar V_d/(V\cos\theta) = (c\hbar\mathcal{E})/(\mathcal{B}V\cos\theta)$ (see Sec. III A). Thus the Kane fermion in crossed electric and magnetic fields decays into two independent Dirac fermions by increasing the electric fields.

Figure 3 provides the Landau level calculations in crossed electric and magnetic fields in HgCdTe bulk crystals with inverted and noninverted band structure for $\mathcal{B} \parallel [001]$ and $\mathcal{E} \parallel [100]$. The latter corresponds to $\phi = 0$ in $\hat{\mathcal{K}}'_t$ and $\hat{\mathcal{K}}'$ defined by Eqs. (25) and (29), respectively. In order to solve the secular equation (38), we applied the five-step iteration procedure involving the truncated matrix composed of $\hat{\mathcal{H}}'_{mn}$ with $N = 50$ terms in the expansion of $|\Phi'_{8\times8}\rangle$ in Eq. (39). Then, solution of the secular equation (38) was transformed into the energies of Landau levels by means of Eq. (44).

The energy of the Landau levels in HgCdTe crystals is plotted in Fig. 3, as a function of magnetic field, in two different regimes. In small magnetic fields exceeding $B_c = (c\hbar\mathcal{E})/(V\cos\theta)$ at which $\beta = 1$, the Landau level energies are reproduced by the picture involving two independent Dirac fermions in accordance with the conclusion made above. Above 3 T, the Dirac fermion regime, characterized by double-degenerated Landau levels [except the one at $n = -1$ in Eq. (71)] progressively transforms into the Kane fermion picture characterized by strong hybridization between light- and heavy-hole bands. In high magnetic fields, corresponding to the small β values, the Landau level energies asymptotically tend to the ones in the absence of electric fields.

A similar behavior of the Landau levels is observed for other orientations of the magnetic field, particularly for $\mathcal{B} \parallel [010]$ shown in Fig. 4. As seen, the only qualitative difference between the Landau levels for $\mathcal{B} \parallel [010]$ and those for $\mathcal{B} \parallel [001]$ discussed above is the smaller range of magnetic fields, in which the Dirac fermion regime is established. This difference is caused by different definitions of ξ_0 for $\mathcal{B} \parallel [001]$ [see Eq. (31)] and $\mathcal{B} \parallel [010]$ [see Eq. (59)]. In the latter case, the Gaussian factor $\exp(-\xi_0^2)$ determining the Landau level evolution with magnetic field is written as

$$e^{-\xi_0^2} = \exp\left[-\frac{\delta^2 a_B^2 (C_2 - C_1)^2}{4V^2 \cos\theta (1-\delta^2)^{3/2}}\right]. \qquad (72)$$

As seen from Fig. 4, the Landau level energies in small magnetic fields [such that $\exp(-\xi_0^2) \to 0$] are defined as

$$E_{\mathrm{Dirac}}^{[010]} = C_{1,2} - \delta V k_y \pm \sqrt{1-\delta^2} \times \sqrt{M_{1,2}^2 + V^2 k_z^2 + \sqrt{1-\delta^2}\frac{2V^2(n+1)\cos\theta}{a_B^2}}, \tag{73}$$

where $n \geqslant -1$ and $\delta = (c\hbar\mathcal{E})/(V\mathcal{B})$ (see Sec. III B).

Thus we can conclude that the Kane fermion in crossed fields always decays into two independent Dirac particles, which is represented by a vanishing of the mixing between the light and heavy hole bands as the magnetic field decreases. The magnetic field range of such Dirac fermion regime is defined by the difference $C_2 - C_1$ and the orientation of electric and magnetic fields with respect to the main crystallographic axes of the zinc-blende crystal. Note that $C_2 - C_1$ is always nonzero due to the band positions in HgCdTe crystals [see Eq. (13)]. We also note that the conclusions above hold in the presence of a gap between the light- and heavy-hole subbands, which includes the uniaxially strained HgCdTe and Cd_3As_2 [42] bulk crystals. As seen from above, the decay of the Kane fermion is absent if the (3+1)-band Hamiltonian preserves the particle-hole symmetry, i.e., at $C_1 = C_2$.

The above conclusions remain valid even beyond the "symmetric approximation" of the (3+1)-band Hamiltonian, i.e., when two Dirac subsystems are characterized by different "speeds of light" $V_1/\hbar$ and $V_2/\hbar$ (see Appendix A). This arises if the interband momentum matrix elements P for Γ_{8v}–Γ_{6c} bands and Q for Γ_{8v}–Γ_{7c} bands differ significantly, which takes place for instance in bulk InSb [43]. The exact solution of the problem when $V_1 \neq V_2$ is a rather cumbersome task and is beyond the scope of this work. Further, we only restrict ourselves to the qualitative algorithm description, following which one can accurately find the Landau levels beyond the symmetric approximation.

If $V_1 \neq V_2$, instead of the "global" Lorentz boost transformation, one must first find the Landau levels in the crossed fields for each of the Dirac subsystems separately. The solution to this problem, in turn, can be performed by means of two "local" Lorentz boost transformations, each characterized by its own speed of light. Then, by using the wave functions in a stationary frame of reference as the basis expansion, one can take into account the coupling between two Dirac subsystems and reduce the Landau level calculations to the corresponding matrix secular equation. By analogy with the symmetric approximation, the secular equation will contain the antidiagonal blocks with the elements proportional to the novel Γ factor [cf. Eq. (42)] defined as

$$\Gamma_{\lambda_1,n_1,\lambda_2,n_2}(\xi_1,\xi_2) = \int_{-\infty}^{+\infty} F_{n_1}(\lambda_1\xi + \xi_1)F_{n_2}(\lambda_2\xi + \xi_2)d\xi, \tag{74}$$

where the presence of λ_1 and λ_2 is due to different speeds of light in the Dirac subsystems [see the definition of ξ for $\mathcal{B} \parallel [001]$ in Eq. (31) and for $\mathcal{B} \parallel [010]$ in Eq. (59)]. Although the integral in Eq. (74) cannot be calculated analytically, it can be shown that

$$\Gamma_{\lambda_1,n_1,\lambda_2,n_2}(\xi_1,\xi_2) \sim \exp\left[-\frac{(\lambda_1\xi_2 + \lambda_2\xi_1)^2}{2(\lambda_1^2+\lambda_2^2)}\right] \tag{75}$$

for any values of n_1 and n_2. If ξ_1 or ξ_2 is large enough, which happens when the magnetic field approaches a critical value of the Landau level collapse in one of the Dirac subsystems, $\Gamma_{\lambda_1,n_1,\lambda_2,n_2}(\xi_1,\xi_2)$ vanishes. Under these conditions, the Kane fermion decays into two independent Dirac particles as in the symmetric case of $V_1 = V_2$ discussed earlier.

Since the fermion decay into two Dirac particles in the (3+1)-band model occurs at any value of M_2 and $0 < \theta < \pi/2$, one can also conclude that the flat band described by $\hat{\mathcal{H}}_{6\times6}(\mathbf{k},\theta)$ in Eq. (1) in the limiting case of $M_2 \to \infty$ becomes fully decoupled from the conical bands when the magnetic field approaches its critical value. This fact in a sense justifies the use of semiclassical approximation within the three-band model (see Sec. II), which ignores the interband coupling. Although the critical magnetic field calculated within the semiclassical approximation is independent from orientation of $\mathcal{B}$, this approach may however qualitatively describe the evolution of Landau levels if $\mathcal{E}$ is used as a fitting parameter. This particularly explains a good agreement between the Landau level transition energies calculated on the basis of Eq. (6) and experimental results on magnetoabsorption of InSb observed by Zawadzki *et al.* [33]. Note that in Ref. [33], $\mathcal{E} \parallel [111]$, while the orientation of $\mathcal{B} \perp \mathcal{E}$ with respect to the main crystallographic axes were unknown, which is different from the two cases of $\mathcal{E} \parallel [100]$ considered in Sec. III.

V. SUMMARY

In conclusion, by taking into account an additional conduction Γ_{7c} band resulting in finite curvature of the heavy-hole band in zinc-blende crystals, we unequivocally identify the Kane fermions as complex spin-1/2 particles composed of two *mutually hybridized* Dirac fermions. The latter allows us to directly apply the Lorentz transformation for the theoretical investigation of the Landau level collapse of Kane fermions in crossed electric and magnetic fields. We have found that increasing the electric field first leads to the decay of the Kane fermion into two independent Dirac particles. Then, the Landau levels of the decayed particles collapse when their drift velocities V_d achieve V_d^* lying between *half* and *whole* values of the effective speed of the light. The latter strongly depends on the orientation of the electric and magnetic fields with respect to the main crystallographic axes of the zinc-blende crystals. This is a distinctive feature of Kane fermions, since the Landau levels of conventional Dirac fermion collapse occurs when V_d approaches the effective speed of the light. Our results pave the way for deep understanding of pseudorelativistic effects in narrow-gap semiconductors arising in crossed electric and magnetic fields.

ACKNOWLEDGMENTS

This work was partially supported by the Foundation for Polish Science: the IRAP program (Grant No. MAB/2018/9, project CENTERA), by CNRS through IRP "TeraMIR", and

by the French Agence Nationale pour la Recherche ("Dirac 3D" and "Colector" projects).

APPENDIX A: (3+1)-BAND MODEL IN CUBIC SEMICONDUCTORS

The most accurate description of the band structure of diamond and zinc-blende semiconductors at the energies close to the fundamental gap can be performed by taking directly into consideration the Γ_{8c}, Γ_{7c}, Γ_{6c}, Γ_{8v}, and Γ_{7v} bands, resulting in the 14×14 $\mathbf{k}\cdot\mathbf{p}$ Hamiltonian [36–38]. In this Hamiltonian, the nonzero curvature of the heavy-hole band stems from the momentum matrix element Q between the valence $\Gamma_{8v} + \Gamma_{7v}$ and conduction $\Gamma_{8c} + \Gamma_{7c}$ bands [37,38].

Before going further, we first note that the splitting at the Γ point of the Brillouin zone between Γ_{8c} and Γ_{7c}, as well as between Γ_{8v} and Γ_{7v}, is caused by the spin-orbit interaction. The latter means that if one considers the case of large spin-orbit interaction, which is a good approximation for narrow-gap HgCdTe [28,29] and InSb [33,34] semiconductors, in addition to the low-lying valence Γ_{7v} band, one should also exclude the high-lying conduction Γ_{8c} band. Under these assumptions, the Hamiltonian for the Γ_{7c}, Γ_{6c}, and Γ_{8v} bands can be presented in the block form:

$$\mathcal{H}_{8\times8}^{(3+1)}(\mathbf{k}) = \begin{pmatrix} \mathcal{H}_{7c7c} & \mathcal{H}_{7c6c} & \mathcal{H}_{7c8v} \\ \mathcal{H}_{6c7c} & \mathcal{H}_{6c6c} & \mathcal{H}_{6c8v} \\ \mathcal{H}_{8v7c} & \mathcal{H}_{8v6c} & \mathcal{H}_{8v8v} \end{pmatrix}. \tag{A1}$$

Neglecting quadratic terms representing the remote band contribution [36–38] and the small terms arising due to the absence of the inversion center in the unit cell of zinc-blende semiconductors [38], the blocks in Eq. (A1) are written as

$$\begin{aligned} \mathcal{H}_{7c7c} &= E_{7c}\sigma_0, \\ \mathcal{H}_{7c6c} &= \mathcal{H}_{6c7c}^{\dagger} = 0, \\ \mathcal{H}_{7c8v} &= \mathcal{H}_{8v7c}^{\dagger} = -2Q(T_{yz}k_x + T_{zx}k_y + T_{xy}k_z), \\ \mathcal{H}_{6c6c} &= E_{6c}\sigma_0, \\ \mathcal{H}_{6c8v} &= \mathcal{H}_{8v6c}^{\dagger} = \sqrt{3}P(T_x k_x + T_y k_y + T_z k_z), \\ \mathcal{H}_{8v8v} &= E_{8v}\begin{pmatrix} \sigma_0 & 0 \\ 0 & \sigma_0 \end{pmatrix}, \end{aligned} \tag{A2}$$

where P is the momentum matrix element between the Γ_{6c} and Γ_{8v} bands, the symbol "†" represents Hermitian conjugation, T_a and T_{ab} are the matrices defined in Ref. [46], and E_{7c}, E_{6c}, and E_{8v} correspond to the energies of the Γ_{7c}, Γ_{6c}, and Γ_{8v} bands, respectively. In Eq. ((A2) 2), the axes are assumed to be oriented as follows: $x \parallel [100]$, $y \parallel [010]$, and $z \parallel [001]$. Note that the given form of $\mathcal{H}_{8v8v}$ in Eq. ((A2) 2) represents the bulk semiconductor in the absence of uniaxial strain. For the latter, one should introduce an additional gap at $\mathbf{k} = 0$ between the light- and heavy-hole bands [39].

The Hamiltonian $\mathcal{H}_{8\times8}^{(3+1)}(\mathbf{k})$ in Eq. (A1) allows one to go beyond the flat-band approximation for the heavy holes (see Fig. 1) and obtain a more realistic description of the band structure for narrow-gap HgCdTe and InSb semiconductors at the energies close to the fundamental gap. One may argue that taking into account the high-lying conduction Γ_{7c} band and simultaneously neglecting the valence Γ_{7v} band is an excess of the accuracy of this model. However, the Γ_{7v} band has no effect on the heavy-hole mass [47], while taking the Γ_{7c} band into account yields the nonzero band curvature of the heavy holes. This can be directly demonstrated by projecting $\mathcal{H}_{8\times8}^{(3+1)}(\mathbf{k})$ on the $\Gamma_{6c} + \Gamma_{8v}$ subspace, which results in the square corrections to the three-band Hamiltonian arising in the diagonal $\mathcal{H}_{8v8v}^{(3\text{-band})}$ block:

$$\begin{aligned} \mathcal{H}_{8v8v}^{(3\text{-band})} = {} & E_{8v}\begin{pmatrix} \sigma_0 & 0 \\ 0 & \sigma_0 \end{pmatrix} \\ & + \frac{\hbar^2}{2m_0}\left[-\left(\gamma_1 + \frac{5}{2}\gamma_2\right)\mathbf{k}^2 + 2\gamma_2(\mathbf{J}\cdot\mathbf{k})^2\right] \\ & + \frac{2\hbar^2}{m_0}(\gamma_3 - \gamma_2)[\{J_xJ_y\}k_xk_y + \{J_yJ_z\}k_yk_z \\ & + \{J_zJ_x\}k_zk_x], \end{aligned} \tag{A3}$$

where m_0 is the free-electron mass, $\mathbf{J}$ is the vector composed of the matrices of the angular momentum 3/2, $\{J_aJ_b\} = (J_aJ_b + J_bJ_a)/2$, and γ_1, γ_2, and γ_3 are the *effective* Luttinger parameters for the three-band $\mathbf{k}\cdot\mathbf{p}$ model defined as

$$\begin{aligned} \gamma_1 &= \frac{1}{3}\frac{2m_0}{\hbar^2}\frac{Q^2}{E_{7c} - E_{8v}}, \\ \gamma_2 &= -\frac{1}{6}\frac{2m_0}{\hbar^2}\frac{Q^2}{E_{7c} - E_{8v}}, \\ \gamma_3 &= \frac{1}{6}\frac{2m_0}{\hbar^2}\frac{Q^2}{E_{7c} - E_{8v}}. \end{aligned} \tag{A4}$$

As is clear, Eq. (A3) represents nothing but the square corrections to the three-band $\mathbf{k}\cdot\mathbf{p}$ Hamiltonian for the Γ_{6c} and Γ_{8v} bands, resulting in the nonzero curvature of the heavy-hole subband. The latter is characterized by anisotropic effective mass m_{hh} defined by the Luttinger parameters [48]. For instance, on the basis of the effective mass along the [100] crystallographic direction

$$\frac{m_0}{m_{hh}^{[100]}} = \gamma_1 - 2\gamma_2 = \frac{2}{3}\frac{2m_0}{\hbar^2}\frac{Q^2}{E_{7c} - E_{8v}}, \tag{A5}$$

one can override parameters Q and $E_{7c} - E_{8v}$ by using the experimental values of γ_1 and γ_2.

The main advantage of $\mathcal{H}_{8\times8}^{(3+1)}(\mathbf{k})$ is its linearity in $\mathbf{k}$, which plays *a key role in understanding of relativistic properties* of Kane fermions. By using the unitary transformation, the Hamiltonian can be presented in the form of two coupled Dirac Hamiltonians:

TABLE I. Band parameters of bulk $Hg_{1-x}Cd_xTe$ crystals at $T = 2$ K in the absence of biaxial strain ($\delta_\epsilon = 0$) used in the (3+1)-band $\mathbf{k}\cdot\mathbf{p}$ model within the "symmetric approximation." Experimental values of $m_{hh}^{[100]}$ and M_1 were calculated on the basis of material parameters provided in Ref. [39]. Other parameters were obtained on the basis of Eq. (A5) by assuming $P = Q$.

x	$m_{hh}^{[100]}/m_{0_{\rm exp}}$	$P_{\rm exp}$ (eV Å)	E_{7c}–E_{8v} (eV)	$V_1 = V_2$ (eV Å)	C_1 (eV)	C_2 (eV)	M_1 (eV)	M_2 (eV)
0.00	0.323	8.46 [29,39]	3.5–4.8 [44,45]	6.91	0.000	2.173	−0.151	2.021
0.10	0.334	8.46 [29,39]		6.91	0.000	2.156	−0.062	2.094
0.14	0.339	8.46 [29,39]		6.91	0.000	2.150	−0.026	2.124
$x_c \simeq 0.168$	0.342	8.46 [29,39]		6.91	0.000	2.146	0	2.146
0.20	0.347	8.46 [29,39]		6.91	0.000	2.143	0.029	2.171
0.25	0.353	8.46 [29,39]		6.91	0.000	2.138	0.075	2.212
0.30	0.360	8.46 [29,39]		6.91	0.000	2.134	0.121	2.255
0.35	0.367	8.46 [29,39]		6.91	0.000	2.132	0.168	2.299

$$\hat{\mathcal{H}}_{8\times8}^{(3+1)}(\mathbf{k}) = \begin{pmatrix} C_1+M_1 & 0 & V_1k_z & \frac{V_1}{2}k_- & 0 & 0 & 0 & \frac{\sqrt{3}V_1}{2}k_+ \\ 0 & C_1+M_1 & \frac{V_1}{2}k_+ & -V_1k_z & 0 & 0 & \frac{\sqrt{3}V_1}{2}k_- & 0 \\ V_1k_z & \frac{V_1}{2}k_- & C_1-M_1 & 0 & 0 & -\frac{\sqrt{3}V_2}{2}k_+ & 0 & 0 \\ \frac{V_1}{2}k_+ & -V_1k_z & 0 & C_1-M_1 & -\frac{\sqrt{3}V_2}{2}k_- & 0 & 0 & 0 \\ 0 & 0 & 0 & -\frac{\sqrt{3}V_2}{2}k_+ & C_2+M_2 & 0 & V_2k_z & \frac{V_2}{2}k_- \\ 0 & 0 & -\frac{\sqrt{3}V_2}{2}k_- & 0 & 0 & C_2+M_2 & \frac{V_2}{2}k_+ & -V_2k_z \\ 0 & \frac{\sqrt{3}V_1}{2}k_+ & 0 & 0 & V_2k_z & \frac{V_2}{2}k_- & C_2-M_2 & 0 \\ \frac{\sqrt{3}V_1}{2}k_- & 0 & 0 & 0 & \frac{V_2}{2}k_+ & -V_2k_z & 0 & C_2-M_2 \end{pmatrix}, \tag{A6}$$

where $k_\pm = k_x \pm ik_y$, $V_1 = \sqrt{2/3}P$, $V_2 = \sqrt{2/3}Q$, and $C_{1,2}$, $M_{1,2}$ are defined from the following equations:

$$\begin{aligned} C_1 + M_1 &= E_{6c}, \quad C_1 - M_1 = E_{8v}, \\ C_2 + M_2 &= E_{7c}, \quad C_2 - M_2 = E_{8v}. \end{aligned} \tag{A7}$$

The last expression determines the position of the heavy-hole band at $\mathbf{k} = 0$. For the case of uniaxial strain or Cd_3As_2, $C_2 - M_2 = E_{8v} + \delta_\epsilon$, where δ_ϵ represents the gap between the light- and heavy-hole subbands [39].

For better understanding the coupling origin between two 4×4 Dirac blocks, we further introduce hybridization angle θ describing the mixing between light- and heavy-hole branches in the Γ_{8v} band [32]. Thus the Hamiltonian $\hat{\mathcal{H}}_{8\times8}^{(3+1)}(\mathbf{k})$ in Eq. (A6) is generalized as

$$\hat{\mathcal{H}}_{8\times8}^{(3+1)}(\mathbf{k}) = \begin{pmatrix} C_1+M_1 & 0 & V_1k_z & V_1k_-\cos\theta & 0 & 0 & 0 & V_1k_+\sin\theta \\ 0 & C_1+M_1 & V_1k_+\cos\theta & -V_1k_z & 0 & 0 & V_1k_-\sin\theta & 0 \\ V_1k_z & V_1k_-\cos\theta & C_1-M_1 & 0 & 0 & -V_2k_+\sin\theta & 0 & 0 \\ V_1k_+\cos\theta & -V_1k_z & 0 & C_1-M_1 & -V_2k_-\sin\theta & 0 & 0 & 0 \\ 0 & 0 & 0 & -V_2k_+\sin\theta & C_2+M_2 & 0 & V_2k_z & V_2k_-\cos\theta \\ 0 & 0 & -V_2k_-\sin\theta & 0 & 0 & C_2+M_2 & V_2k_+\cos\theta & -V_2k_z \\ 0 & V_1k_+\sin\theta & 0 & 0 & V_2k_z & V_2k_-\cos\theta & C_2-M_2 & 0 \\ V_1k_-\sin\theta & 0 & 0 & 0 & V_2k_+\cos\theta & -V_2k_z & 0 & C_2-M_2 \end{pmatrix}, \tag{A8}$$

where $\theta = \pi/3$ corresponds to the case of Kane fermions [32] in narrow-gap HgCdTe and InSb semiconductors, while $\theta = 0$ represents the case of two independent Dirac particles.

Finally, the Hamiltonian in Eq. (A8) can be further simplified for HgCdTe crystals by setting $V_1 \simeq V_2$. As seen from Table I, only the Luttinger parameters and the values of P are well known for HgCdTe semiconductors, while the scatter of the energies $E_{7c} - E_{8v}$ for HgTe is quite large in comparison with the band gap $E_{6c} - E_{8v} = 2M_1$ [39]. Converting the scatter range of $E_{7c} - E_{8v}$ into the range of the Q values by means of Eq. (A5) with the known mass $m_{hh}^{[100]}$, one can find that Q should change between 7.87 eV Å and 9.22 eV Å for HgTe. Since the Q ranges overlap with the P values in Table I, one can indeed apply symmetric approximation for $\hat{\mathcal{H}}_{8\times8}^{(3+1)}(\mathbf{k})$ in narrow-gap HgCdTe semiconductors by setting $P \simeq Q$ and therefore $V_1 \simeq V_2$. Thus, in the calculations on the basis of the (3+1)-band Hamiltonian, it is preferable to use $P = Q = 8.46$ eV Å, resulting in $E_{7c} - E_{8v} = 4.042$ eV for HgTe. The values of $E_{7c} - E_{8v}$ for $Hg_xCd_{1-x}Te$ alloys can be calculated by assuming the linear variation of the Luttinger parameters with x [39] and $P = Q = 8.64$ eV Å independent of x [29].

In the symmetric approximation, the Hamiltonian in Eq. (A8) can be written in a more compact form:

$$\hat{\mathcal{H}}^{(3+1)}_{8\times8}(\mathbf{k}) = \begin{pmatrix} \hat{\mathcal{H}}^{(1)}_D(\mathbf{k}) & V\ \sin\theta(k_x\beta_y - k_y\beta_x) \\ V\ \sin\theta(k_y\beta_x - k_x\beta_y) & \hat{\mathcal{H}}^{(2)}_D(\mathbf{k}) \end{pmatrix}, \tag{A9}$$

where $\hat{\mathcal{H}}^{(1,2)}_D(\mathbf{k})$ are

$$\hat{\mathcal{H}}^{(1,2)}_D(\mathbf{k}) = C_{1,2}\mathcal{I}_4 + M_{1,2}\alpha_0 + V\ \cos\theta(k_x\alpha_x + k_y\alpha_y) + Vk_z\alpha_z, \tag{A10}$$

where $\mathcal{I}_4$ is a 4×4 identity matrix and the α and β matrices are related to the Pauli matrices as

$$\alpha_0 = \begin{pmatrix} \sigma_0 & 0 \\ 0 & -\sigma_0 \end{pmatrix}, \quad \alpha_{x,y,z} = \begin{pmatrix} 0 & \sigma_{x,y,z} \\ \sigma_{x,y,z} & 0 \end{pmatrix},$$
$$\beta^{(z)}_0 = \begin{pmatrix} i\sigma_z & 0 \\ 0 & -i\sigma_z \end{pmatrix}, \quad \beta_{x,y} = \begin{pmatrix} 0 & \sigma_{y,x} \\ -\sigma_{y,x} & 0 \end{pmatrix}. \tag{A11}$$

The expediency of introducing the β matrices in this form is due to their transformation upon Lorentz boost along the y axis, $L^{(y)}_{4\times4}(\alpha) = \exp(\alpha_y\cdot\alpha/2)$:

$$\begin{aligned} L^{(y)}_{4\times4}(\alpha)\beta^{(z)}_0 L^{(y)}_{4\times4}(\alpha) &= \beta^{(z)}_0\cosh\alpha + \beta_y\sinh\alpha, \\ L^{(y)}_{4\times4}(\alpha)\beta_y L^{(y)}_{4\times4}(\alpha) &= \beta_y\cosh\alpha + \beta^{(z)}_0\sinh\alpha, \\ L^{(y)}_{4\times4}(\alpha)\beta_x L^{(y)}_{4\times4}(\alpha) &= \beta_x. \end{aligned} \tag{A12}$$

Note the indices order in the definition of β_x and β_y.

APPENDIX B: (3+1)-BAND MODEL FOR ARBITRARY ORIENTATIONS OF ELECTRIC AND MAGNETIC FIELDS

Up to now, the x, y, and z axes are assumed to be oriented along the main crystallographic directions, namely [100] and [010] and [001], respectively. Further, we consider a more general case when the magnetic field $\mathcal{B}$ is oriented along the new z' axis deflected at angle θ_0 to the [001] direction, while electric field $\mathcal{E}$ is tilted at angle ϕ from the [100] direction as shown in Fig. 5.

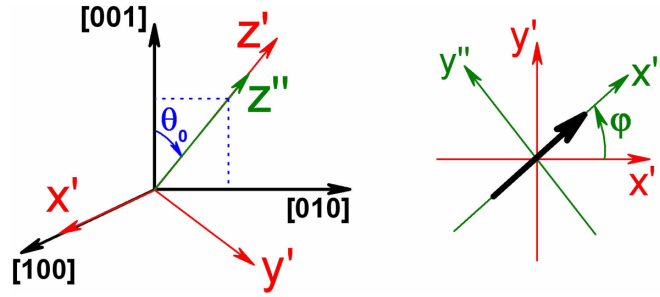

FIG. 5. Left panel: mutual orientation of two Cartesian axes (x', y', z') and (x'', y'', z'') with respect to the main crystallographic axes. Right panel: the orientation of electric field $\mathcal{E}$ (shown by black arrow) in the Cartesian axes.

To write the Hamiltonian in Eq. (A9) in the new coordinate system, one has to rotate the electron momentum around the [100] axis, and then around the new axis z' in accordance with the transformations

$$\begin{pmatrix} k_x \\ k_y \\ k_z \end{pmatrix} = \begin{pmatrix} 1 & 0 & 0 \\ 0 & \cos\theta_0 & -\sin\theta_0 \\ 0 & \sin\theta_0 & \cos\theta_0 \end{pmatrix}\begin{pmatrix} k_{x'} \\ k_{y'} \\ k_{z'} \end{pmatrix} \tag{B1}$$

and

$$\begin{pmatrix} k_{x'} \\ k_{y'} \\ k_{z'} \end{pmatrix} = \begin{pmatrix} \cos\phi & -\sin\phi & 0 \\ \sin\phi & \cos\phi & 0 \\ 0 & 0 & 1 \end{pmatrix}\begin{pmatrix} k_{x''} \\ k_{y''} \\ k_{z''} \end{pmatrix}. \tag{B2}$$

Simultaneously with the transition from (k_x, k_y, k_z) to ($k_{x''}$, $k_{y''}$, $k_{z''}$), one should also apply a unitary transformation to the Hamiltonian (A9):

$$\hat{\mathcal{H}}''^{(3+1)}_{8\times8}(\mathbf{k}'') = U^{-1}_z(\phi)U^{-1}_x(\theta_0)\hat{\mathcal{H}}^{(3+1)}_{8\times8}(\mathbf{k})U_x(\theta_0)U_z(\phi), \tag{B3}$$

where $U_x(\theta_0)$ and $U_z(\phi)$ are defined as

$$U_x(\theta_0) = \mathcal{I}_4\otimes\exp(i\sigma_x\cdot\theta_0/2),$$
$$U_z(\phi) = \mathcal{I}_4\otimes\exp(i\sigma_z\cdot\phi/2).$$

After all the calculations, the Hamiltonian $\hat{\mathcal{H}}''^{(3+1)}_{8\times8}(\mathbf{k}'')$ in the new coordinate system takes the form

$$\hat{\mathcal{H}}''^{(3+1)}_{8\times8}(\mathbf{k}'') = \begin{pmatrix} \hat{\mathcal{H}}''^{(1)}_D(\mathbf{k}'') & V\ \sin\theta\hat{\mathcal{K}}''(\mathbf{k}'') \\ -V\ \sin\theta\hat{\mathcal{K}}''(\mathbf{k}'') & \hat{\mathcal{H}}''^{(2)}_D(\mathbf{k}'') \end{pmatrix}, \tag{B4}$$

where the blocks $\hat{\mathcal{H}}''^{(1,2)}_D(\mathbf{k}'')$ and $\hat{\mathcal{K}}''(\mathbf{k}'')$ are written as

$$\begin{aligned} \hat{\mathcal{H}}''^{(1,2)}_D(\mathbf{k}'') &= C_{1,2}\mathcal{I}_4 + M_{1,2}\alpha_0 + V\ \cos\theta(k_{x''}\alpha_{x''} + k_{y''}\alpha_{y''}) + Vk_{z''}\alpha_{z''} \\ &+ (1-\cos\theta)Vk_{x''}\left(\alpha_{x''}\sin^2\theta_0\sin^2\phi + \alpha_{y''}\frac{\sin^2\theta_0\sin2\phi}{2} + \alpha_{z''}\frac{\sin2\theta_0\sin\phi}{2}\right) \\ &+ (1-\cos\theta)Vk_{y''}\left(\alpha_{x''}\frac{\sin^2\theta_0\sin2\phi}{2} + \alpha_{y''}\sin^2\theta_0\cos^2\phi + \alpha_{z''}\frac{\sin2\theta_0\cos\phi}{2}\right) \\ &+ (1-\cos\theta)Vk_{z''}\left(\alpha_{x''}\frac{\sin2\theta_0\sin\phi}{2} + \alpha_{y''}\frac{\sin2\theta_0\cos\phi}{2} - \alpha_{z''}\sin^2\theta_0\right) \end{aligned} \tag{B5}$$

and

$$\hat{\mathcal{K}}''(\mathbf{k}'') = k_{x''}\left(-\beta_{x''}\frac{(1+\cos^2\theta_0)\sin 2\phi}{2} + \beta_{y''}\left(\cos^2\phi - \cos^2\theta_0\sin^2\phi\right) + \beta_{z''}\frac{\sin 2\theta_0\sin\phi}{2}\right)$$
$$+ k_{y''}\left(\beta_{x''}(\sin^2\phi - \cos^2\theta_0\cos^2\phi) - \beta_{y''}\frac{(1+\cos^2\theta_0)\sin 2\phi}{2} + \beta_{z''}\frac{\sin 2\theta_0\cos\phi}{2}\right)$$
$$+ k_{z''}\left(\beta_{x''}\frac{\sin 2\theta_0\cos\phi}{2} + \beta_{y''}\frac{\sin 2\theta_0\sin\phi}{2} - \beta_{z''}\sin^2\theta_0\right), \tag{B6}$$

where we have additionally introduced $\beta_{z''}$ as

$$\beta_{z''} = \begin{pmatrix} 0 & \sigma_{z''} \\ -\sigma_{z''} & 0 \end{pmatrix}. \tag{B7}$$

Further and in the main text, we omit the prime marks keeping in mind that orientation of new x, y, and z axes does not coincide with the main crystallographic directions in the most general case.

If z is oriented along the [001] direction ($\theta_0 = 0$; see Sec. III A), $\hat{\mathcal{H}}_D^{(1,2)}(\mathbf{k})$ takes the form of Eq. (A10), while $\hat{\mathcal{K}}(\mathbf{k})$ is written as

$$\hat{\mathcal{K}}(\mathbf{k}) = (k_x\beta_y - k_y\beta_x)\cos 2\phi - (k_x\beta_x + k_y\beta_y)\sin 2\phi. \tag{B8}$$

In this case, the x and y orientations relative to the main crystallographic directions are determined by the angle ϕ as shown in Fig. 5. For the particular case of $x \parallel [100]$, $y \parallel [00\bar{1}]$, and $z \parallel [010]$ ($\theta_0 = \pi/2$ and $\phi = 0$; see Sec. III B), $\hat{\mathcal{H}}_D^{(1,2)}(\mathbf{k})$ and $\hat{\mathcal{K}}(\mathbf{k})$ have the form

$$\hat{\mathcal{H}}_D^{(1,2)}(\mathbf{k}) = C_{1,2}\mathcal{I}_4 + M_{1,2}\alpha_0 + V\cos\theta k_x\alpha_x + Vk_y\alpha_y + V\cos\theta k_z\alpha_z \tag{B9}$$

and

$$\hat{\mathcal{K}}(\mathbf{k}) = k_x\beta_y - k_z\beta_z. \tag{B10}$$

APPENDIX C: COLLAPSE of LANDAU LEVELS AT ARBITRARY ORIENTATIONS OF ELECTRIC AND MAGNETIC FIELDS

Let us now find the drift velocity V_d for an arbitrary orientation of magnetic field (and electric field $\mathcal{E} \perp \mathcal{B}$), at which the collapse of the Landau levels occurs. Assuming the orientation of electric field $\mathcal{E}$ in the x direction and magnetic field $\mathcal{B}$ in the z direction, the Schrödinger equation with the Hamiltonian (B4) characterized by the arbitrary orientation of the Cartesian axes with respect to the main crystallographic directions is written as

$$\left[\hat{\mathcal{H}}_{8\times 8}^{(3+1)}\left(\hat{k}_x, k_y + \frac{x}{a_B^2}, k_z\right) + \left(-i\hbar\frac{\partial}{\partial t} + e\mathcal{E}x\right)\mathcal{I}_8\right]|\Psi_{8\times 8}\rangle = 0, \tag{C1}$$

where $\hat{k}_x = -i\partial/\partial x$.

As shown in Sec. III, the Landau level collapse is defined by the parameter α^* of the Lorentz boost along the y axis. As is clear, the elimination of electric field $\mathcal{E}$ in the moving reference frame is caused by the terms proportional to $k_y\alpha_y$ in the Dirac blocks (B5), namely by $\Lambda(\theta, \theta_0, \phi)Vk_y\alpha_y$, where

$$\Lambda(\theta, \theta_0, \phi) = \cos\theta + \sin^2\theta_0\cos^2\phi(1 - \cos\theta). \tag{C2}$$

Then, introducing the time-momentum operator k_t as $V\Lambda(\theta, \theta_0, \phi)k_t = -i\hbar\partial/\partial t$, one can show that the term $k_t\mathcal{I}_4 + k_y\alpha_y$ in two diagonal blocks of Eq. (C1) remains invariant upon the Lorentz transformation, i.e.,

$$(k_t\mathcal{I}_4 + k_y\alpha_y) \longrightarrow \left(k_t'\mathcal{I}_4 + k_y'\alpha_y\right), \tag{C3}$$

if (k_t, k_y) are connected with (k_t', k_y') by Eq. (20).

On the contrary, the terms proportional to x in the diagonal blocks of Eq. (C1)

$$e\mathcal{E}x\mathcal{I}_4 + \Lambda(\theta, \theta_0, \phi)V\frac{x}{a_B^2}\alpha_y$$

are transformed as

$$(\beta^*\mathcal{I}_4 + \alpha_y) \to \left[(\sinh\alpha^* + \beta^*\cosh\alpha^*)\mathcal{I}_4 + (\cosh\alpha^* + \beta^*\sinh\alpha^*)\alpha_y\right], \tag{C4}$$

where β^* is introduced as

$$\beta^* = \frac{1}{\Lambda(\theta, \theta_0, \phi)}\frac{c\hbar}{V}\frac{\mathcal{E}}{\mathcal{B}}. \tag{C5}$$

Choosing $\tanh\alpha^* = -\beta^*$ and $\cosh\alpha^* = 1/\sqrt{1-\beta^{*2}}$, we completely remove the terms depending on x from the main diagonal of the matrix Schrödinger equation in the moving reference frame. The latter now contains the effective magnetic field $\mathcal{B}' = \mathcal{B}\sqrt{1-\beta^{*2}}$ and additional terms dependent on β^* [cf. Eqs. (22) and (52)]. Solving the Schrödinger equation in the boosted frame, in the manner described in the main text, and then passing to the original reference frame, we can conclude that the collapse of the Landau levels occurs if $\beta^* = 1$. This condition can be also represented in terms of drift velocity $V_d = c\mathcal{E}/\mathcal{B}$ as

$$V_d = \frac{V}{\hbar}[\cos\theta + \sin^2\theta_0\cos^2\phi(1 - \cos\theta)]. \tag{C6}$$

[1] L. V. Keldysh, Sov. Phys. JETP **18**, 253 (1964).
[2] P. A. Wolff, J. Phys. Chem. Solids **25**, 1057 (1964).
[3] K. S. Novoselov, A. K. Geim, S. V. Morozov, D. Jiang, M. I. Katsnelson, I. V. Grigorieva, S. V. Dubonos, and A. A. Firsov, Nature (London) **438**, 197 (2005).
[4] S. S. Krishtopenko, W. Knap, and F. Teppe, Sci. Rep. **6**, 30755 (2016).
[5] M. Marcinkiewicz, S. Ruffenach, S. S. Krishtopenko, A. M. Kadykov, C. Consejo, D. B. But, W. Desrat, W. Knap, J. Torres, A. V. Ikonnikov, K. E. Spirin, S. V. Morozov, V. I. Gavrilenko, N. N. Mikhailov, S. A. Dvoretskii, and F. Teppe, Phys. Rev. B **96**, 035405 (2017).
[6] S. S. Krishtopenko, S. Ruffenach, F. Gonzalez-Posada, G. Boissier, M. Marcinkiewicz, M. A. Fadeev, A. M. Kadykov, V. V. Rumyantsev, S. V. Morozov, V. I. Gavrilenko, C. Consejo, W. Desrat, B. Jouault, W. Knap, E. Tournié, and F. Teppe, Phys. Rev. B **97**, 245419 (2018).
[7] S. S. Krishtopenko and F. Teppe, Sci. Adv. **4**, eaap7529 (2018).
[8] S. S. Krishtopenko, W. Desrat, K. E. Spirin, C. Consejo, S. Ruffenach, F. Gonzalez-Posada, B. Jouault, W. Knap, K. V. Maremyanin, V. I. Gavrilenko, G. Boissier, J. Torres, M. Zaknoune, E. Tournié, and F. Teppe, Phys. Rev. B **99**, 121405(R) (2019).
[9] D. Hsieh, D. Qian, L. Wray, Y. Xia, Y. S. Hor, R. J. Cava, and M. Z. Hasan, Nature (London) **452**, 970 (2008).
[10] H. Zhang, C.-X. Liu, X.-L. Qi, X. Dai, Z. Fang, and S.-C. Zhang, Nat. Phys. **5**, 438 (2009).
[11] B. A. Assaf, T. Phuphachong, V. V. Volobuev, A. Inhofer, G. Bauer, G. Springholz, L. A. de Vaulchier, and Y. Guldner, Sci. Rep. **6**, 20323 (2016).
[12] Z. K. Liu, B. Zhou, Y. Zhang, Z. J. Wang, H. M. Weng, D. Prabhakaran, S.-K. Mo, Z. X. Shen, Z. Fang, X. Dai, Z. Hussain, and Y. L. Chen, Science **343**, 864 (2014).
[13] Z. K. Liu, J. Jiang, B. Zhou, Z. J. Wang, Y. Zhang, H. M. Weng, D. Prabhakaran, S.-K. Mo, H. Peng, P. Dudin, T. Kim, M. Hoesch, Z. Fang, X. Dai, Z. X. Shen, D. L. Feng, Z. Hussain, and Y. L. Chen, Nat. Mater. **13**, 677 (2014).
[14] M. Neupane, S.-Y. Xu, R. Sankar, N. Alidoust, G. Bian, C. Liu, I. Belopolski, T.-R. Chang, H.-T. Jeng, H. Lin, A. Bansil, F. Chou, and M. Z. Hasan, Nat. Commun. **5**, 3786 (2014).
[15] W. Desrat, S. S. Krishtopenko, B. A. Piot, M. Orlita, C. Consejo, S. Ruffenach, W. Knap, A. Nateprov, E. Arushanov, and F. Teppe, Phys. Rev. B **97**, 245203 (2018).
[16] B. Q. Lv, N. Xu, H. M. Weng, J. Z. Ma, P. Richard, X. C. Huang, L. X. Zhao, G. F. Chen, C. E. Matt, F. Bisti, V. N. Strocov, J. Mesot, Z. Fang, X. Dai, T. Qian, M. Shi, and H. Ding, Nat. Phys. **11**, 724 (2015).
[17] L. X. Yang, Z. K. Liu, Y. Sun, H. Peng, H. F. Yang, T. Zhang, B. Zhou, Y. Zhang, Y. F. Guo, M. Rahn, D. Prabhakaran, Z. Hussain, S.-K. Mo, C. Felser, B. Yan, and Y. L. Chen, Nat. Phys. **11**, 728 (2015).
[18] S.-Y. Xu, N. Alidoust, I. Belopolski, Z. Yuan, G. Bian, T.-R. Chang, H. Zheng, V. N. Strocov, D. S. Sanchez, G. Chang, C. Zhang, D. Mou, Y. Wu, L. Huang, C.-C. Lee, S.-M. Huang, B. Wang, A. Bansil, H.-T. Jeng, T. Neupert *et al.*, Nat. Phys. **11**, 748 (2015).
[19] A. G. Aronov and G. E. Pikus, Sov. Phys. JETP **24**, 188 (1967).
[20] A. G. Aronov and G. E. Pikus, Sov. Phys. JETP **24**, 339 (1967).
[21] W. Zawadzki and B. Lax, Phys. Rev. Lett. **16**, 1001 (1966).
[22] M. H. Weiler, W. Zawadzki, and B. Lax, Phys. Rev. **163**, 733 (1967).
[23] V. Lukose, R. Shankar, and G. Baskaran, Phys. Rev. Lett. **98**, 116802 (2007).
[24] A. A. Burkov, M. D. Hook, and L. Balents, Phys. Rev. B **84**, 235126 (2011).
[25] A. A. Soluyanov, D. Gresch, Z. Wang, Q. Wu, M. Troyer, X. Dai, and B. A. Bernevig, Nature (London) **527**, 495 (2015).
[26] B. J. Wieder, Y. Kim, A. M. Rappe, and C. L. Kane, Phys. Rev. Lett. **116**, 186402 (2016).
[27] B. Bradlyn, J. Cano, Z. Wang, M. G. Vergniory, C. Felser, R. J. Cava, and B. A. Bernevig, Science **353**, aaf5037 (2016).
[28] M. Orlita, D. M. Basko, M. S. Zholudev, F. Teppe, W. Knap, V. I. Gavrilenko, N. N. Mikhailov, S. A. Dvoretskii, P. Neugebauer, C. Faugeras, A.-L. Barra, G. Martinez, and M. Potemski, Nat. Phys. **10**, 233 (2014).
[29] F. Teppe, M. Marcinkiewicz, S. S. Krishtopenko, S. Ruffenach, C. Consejo, A. M. Kadykov, W. Desrat, D. But, W. Knap, J. Ludwig, S. Moon, D. Smirnov, M. Orlita, Z. Jiang, S. V. Morozov, V. Gavrilenko, N. N. Mikhailov, and S. A. Dvoretskii, Nat. Commun. **7**, 12576 (2016).
[30] J. D. Malcolm and E. J. Nicol, Phys. Rev. B **92**, 035118 (2015).
[31] A. Raoux, M. Morigi, J.-N. Fuchs, F. Piéchon, and G. Montambaux, Phys. Rev. Lett. **112**, 026402 (2014).
[32] S. S. Krishtopenko, M. Antezza, and F. Teppe, J. Phys.: Condens. Matter **32**, 165501 (2020).
[33] W. Zawadzki, S. Klahn, and U. Merkt, Phys. Rev. Lett. **55**, 983 (1985).
[34] W. Zawadzki, S. Klahn, and U. Merkt, Phys. Rev. B **33**, 6916 (1986).
[35] I. M. Lifshitz and M. I. Kaganov, Sov. Phys. Usp. **2**, 831 (1960).
[36] U. Rössler, Solid State Commun. **49**, 943 (1984).
[37] P. Pfeffer and W. Zawadzki, Phys. Rev. B **41**, 1561 (1990).
[38] H. Mayer and U. Rössler, Phys. Rev. B **44**, 9048 (1991).
[39] S. S. Krishtopenko, I. Yahniuk, D. B. But, V. I. Gavrilenko, W. Knap, and F. Teppe, Phys. Rev. B **94**, 245402 (2016).
[40] N. Gutiérrez Jiménez and S. M. Torba, Appl. Math. Comput. **370**, 124911 (2020).
[41] I. Gradshteyn and I. Ryzhik, *Table of Integrals, Series, and Products* (Elsevier–Academic Press, New York, 1980).
[42] A. Akrap, M. Hakl, S. Tchoumakov, I. Crassee, J. Kuba, M. O. Goerbig, C. C. Homes, O. Caha, J. Novák, F. Teppe, W. Desrat, S. Koohpayeh, L. Wu, N. P. Armitage, A. Nateprov, E. Arushanov, Q. D. Gibson, R. J. Cava, D. van der Marel, B. A. Piot *et al.*, Phys. Rev. Lett. **117**, 136401 (2016).
[43] R. Winkler, *Spin-Orbit Coupling Effects in Two-Dimensional Electron and Hole Systems* (Springer-Verlag, Berlin, 2003).
[44] Semiconductors: Data Handbook, *edited by O. Madelung* (Springer-Verlag, Berlin, 2004).
[45] A. Svane, N. E. Christensen, M. Cardona, A. N. Chantis, M. van Schilfgaarde, and T. Kotani, Phys. Rev. B **84**, 205205 (2011).
[46] H. R. Trebin, U. Rössler, and R. Ranvaud, Phys. Rev. B **20**, 686 (1979).
[47] E. O. Kane, J. Phys. Chem. Solids **1**, 249 (1957).
[48] J. M. Luttinger and W. Kohn, Phys. Rev. **97**, 869 (1955).